

8-11-2007

Multi-Objective Design Optimization Using Metamodelling Techniques and a Damage Material Model

Kenneth Eugene Brister

Follow this and additional works at: <https://scholarsjunction.msstate.edu/td>

Recommended Citation

Brister, Kenneth Eugene, "Multi-Objective Design Optimization Using Metamodelling Techniques and a Damage Material Model" (2007). *Theses and Dissertations*. 3232.
<https://scholarsjunction.msstate.edu/td/3232>

This Graduate Thesis - Open Access is brought to you for free and open access by the Theses and Dissertations at Scholars Junction. It has been accepted for inclusion in Theses and Dissertations by an authorized administrator of Scholars Junction. For more information, please contact scholcomm@msstate.libanswers.com.

MULTI-OBJECTIVE DESIGN OPTIMIZATION USING
METAMODELLING TECHNIQUES AND A
DAMAGE MATERIAL MODEL

By

Kenneth E. Brister

A Thesis
Submitted to the Faculty of
Mississippi State University
in Partial Fulfillment of the Requirements
for the Degree of Master of Science
in Mechanical Engineering
in the Department of Mechanical Engineering

Mississippi State, Mississippi

August 2007

MULTI-OBJECTIVE DESIGN OPTIMIZATION USING
METAMODELING TECHINQUES AND A
DAMAGE MATERIAL MODEL

By

Kenneth E. Brister

Approved:

Mark F. Horstemeyer
Center for Advanced Vehicular Systems
Chair in Computational Solid Mechanics
Professor of Mechanical Engineering
(Major Professor)

Philip M. Gullett
Associate Professor of Civil Engineering
(Committee Member)

Steven R. Daniewicz
Professor of Mechanical Engineering
(Committee Member)

Steven R. Daniewicz
Graduate Coordinator of the Department
of Mechanical Engineering

Glenn Steele
Interim Dean of James Worth Bagley
College of Engineering

Name: Kenneth E. Brister

Date of Degree: August 11, 2007

Institution: Mississippi State University

Major Field: Mechanical Engineering

Major Professor: Dr. Mark F. Horstemeyer

Title of Study: MULTI-OBJECTIVE DESIGN OPTIMIZATION USING
METAMODELING TECHNIQUES AND A DAMAGE
MATERIAL MODEL

Pages in study: 73

Candidate for degree of Master of Science

In this work, the effectiveness of multi-objective design optimization using metamodeling techniques and an internal state variable (ISV) plasticity damage material model as a design tool is demonstrated. Multi-objective design optimization, metamodeling, and ISV plasticity damage material models are brought together to provide a design tool capable of meeting the stringent structural design requirements of today and of the future. The process of implementing this tool are laid out, and two case studies using multi-objective design optimization were carried out. The first was the optimization of a Chevrolet Equinox rear subframe. The optimized subframe was 12% lighter and met design requirements not achieved by the heavier initial design. The second case was the optimization of a Formula SAE front upright. The optimized upright meets all the design constraints and is 22% lighter.

ACKNOWLEDGMENTS

I would like to thank all those who have helped make this Master's Thesis possible. First, I would like to thank my advisor Dr. Mark Horstemeyer who took me on as his student and has patiently support me throughout the past two years. Dr. Horstemeyer has driven me to always look at the big picture and always do my best. I would like thank to David Oglesby for his help and advice. David has provided me with encouragement when things have not gone according to plan. I would like to thank Kiran Solanki and Erdem Acar for all their help with running simulations and optimization codes. Both of these guys have gone out of their way to help me numerous times. I would like to thank all my family and friends for their patience and support. Success means little without people to share it with, and I am glad to have great family and friends to share this accomplishment with. Finally, I want to thank my Lord and Savior for His endless grace. He has truly blessed me.

TABLE OF CONTENTS

ACKNOWLEDGMENTS	ii
LIST OF TABLES.....	v
LIST OF FIGURES	vi
CHAPTER	
I. INTRODUCTION.....	1
II. METAMODELING	7
III. MATERIAL MODEL.....	13
Introduction	13
Plasticity Model Formulation.....	14
Damage Model Formulation	17
Numerical Implementation.....	24
IV. MULTI-OBJECTIVE DESIGN OPTIMIZATION PROCESS	29
Introduction	29
Process.....	32
V. CHEVROLET EQUINOX REAR SUBFRAME CASESTUDY.....	38
Introduction	38
Subframe Construction.....	40
Subframe Finite Element Simulation	41
Subframe Optimization	42
Optimization Results	45
Conclusion.....	49

VI. FORMULA SAE UPRIGHT CASESTUDY	50
Introduction	50
Initial Upright Design.....	52
Upright Optimization	54
Optimization Results	58
Conclusion.....	63
VII. CONCLUSION AND SUMMARY.....	64
REFERENCES	66
APPENDIX	
A FORMULA SAE UPRIGHT LOAD CALCULATIONS	68

LIST OF TABLES

TABLE	Page
5.1. Taguchi L_{27} design of experiments used of subframe optimization.....	43
5.2. Initial and optimized design variable values in millimeters	46
6.1. Initial upright design variable values and starting point values in millimeters.	55
6.2. Taguchi L_{27} DOE used for front upright optimization (all values are in millimeters)	56
6.3. Optimized and initial design variable values given in millimeters.....	58
6.4. Finite element responses for both the optimized and initial upright designs.	58

LIST OF FIGURES

FIGURE	Page
1.1 Types of geometry parameterization: (a) sizing, (b) shape, and (c) topology (Saitou <i>et al.</i> , 2005).	3
1.2. Typical manufacturing and in-service design scenarios (Horstemeyer and Wang, 2003).	5
2.1. Beam example (Jin, Chen, and Simpson, 2002).	8
2.2. Comparison of the RSM and RBF models to the true function (Fang and Horstemeyer, 2006).....	11
3.1. Schematic of the fictitious material with (a) increasing void nucleation (b) increasing void growth and (c) occurrence of void coalescence (Horstemeyer <i>et al.</i> , 2000).	19
3.2. Schematic of the fictitious material with increasing nucleation density and void growth of a model framework (Horstemeyer, 2000)	20
3.3. Radial return algorithm used to update new state as predicted by model (Horstemeyer, 2001).	26
4.1. Simulation based design optimization process flowchart.	30
4.2. Multi-objective design optimization flow chart.....	32
4.3. Beam example (Jin, Chen, and Simpson, 2002).	33
4.4. Example design of experiments with responses.	34
4.5. Design optimization overview.	37
5.1. (a) Original Equinox drivetrain and rear subframe and (b) Challenge X designed electric drivetrain and rear subframe.	39

5.2. (a) OEM cradle design and (b) Challenge X cradle design.	40
5.3. Chevrolet Equinox rear subframe optimization design variables.	42
5.4. Additional material added to reduce stress concentration where control bracket meets transfers tube.....	46
5.5. Optimized cradle (a) displacement from 0.5G Rev Panic brake load case and (b) and (c) stress from 2G/2G Bump load case.	47
5.6. Initial cradle (a) displacement from 0.5G Rev Panic brake load case and (b) and (c) stress from 2G/2G Bump load case.	48
6.1. Formula SAE front upright assembly with control arms and brake rotor and caliber.....	51
6.2. Formula SAE front upright shown with no parts assembled.	51
6.3. The 2006 Formula SAE front upright design (a) and the 2007 front upright design (b).	53
6.4. Front upright optimization design variables.	54
6.5 Stress contour plot for 1.5G cornering load for optimized design in MPa.	59
6.6 Stress contour plot for 1.5G cornering load for initial design in MPa.....	60
6.7. Damage (SDV10) contour plots for 1.25G braking load case for optimized design.	61
6.8. Damage (SDV10) contour plots for 1.25G braking load case for initial design.....	62
A.1. Vehicle center of gravity location and critical dimensions.....	72
A.2. Freebody diagram of Upright 1.25g Braking Loads.....	73
A.3. Freebody diagram of Upright 1.5g Cornering Loads.....	73

CHAPTER I

INTRODUCTION

Design optimization has become a topic of growing importance in advanced vehicular systems design such as in automobiles and aircraft. Each year design requirements are stricken in order to produce lighter, safer, and less expensive vehicles. The National Highway Traffic Safety Administration (2006) reported in their study that 43,340 people were killed in automobile crashes in 2002 alone and that vehicle traffic crashes were a leading cause of death in the United State. Hence, the need for safer automotive designs is ever so present. The demand for lighter vehicles is present along with the need for safer automobiles. With soaring oil prices and tougher EPA restrictions, automakers are looking to reduce weight in all areas in order to produce more fuel efficient and more environmentally friendly vehicles. For every 12% of reduced weight, there is a 10% increase in fuel economy (USAMP, 2006). In order to meet these stringent design requirements, automotive and aerospace producers will have to look at more advanced system designs. Such advanced designs will require an increase in the scope of the design. And, therefore an increase in the design time will lead to higher product cost. As such, a design tool is needed that will streamline the extensive design process. One such tool is multi-objective design optimization.

In order to optimize structural designs, prototyping and physical testing have been utilized historically. An ever increasing drive for lower product cost and shorter development time has lead to the use of finite element analysis (FEA) and computer-aided design (CAD) software. Advances in these tools have made way for the modern computer-aided engineering techniques used today. While FEA has done much to reduce product development time, simulation based optimization is an iterative process that requires a great deal of human interaction and will rarely (if ever) produce the true optimum design. In order to meet and exceed design requirements while reducing product development time, a multi-objective design optimization technique is warranted. Multi-objective design optimization is a parallel process that will consider multiple load conditions while meeting all design objectives.

There are several types of structural design optimization. Design optimization methods can be classified by what type of geometry parameterization they utilize. Saitou *et al.*, (2005) points out three main divisions of geometry parameterization: size, shape, and topology. Size parameterization uses a set of predefined variables to describe the product. This type of parameterization is used mostly for detailed design where only fine tuning is needed. Sizing optimization is a relatively straightforward task, since it typically requires no remeshing of finite element models during optimization iterations (Saitou *et al.*, 2005). Shape optimization allows for more changes in the geometry than size optimization by allowing the boundary of the part geometry to change. Since the part geometry can change dramatically during the process, automatic remeshing of finite element models is usually required (Saitou *et al.*, 2005). The third type, topology

optimization, allows changes in topology in addition to shape so pockets can be placed in the geometry (Saitou *et al.*, 2005). Fig 1.1 illustrates the size, shape, and topology geometry parameterizations.

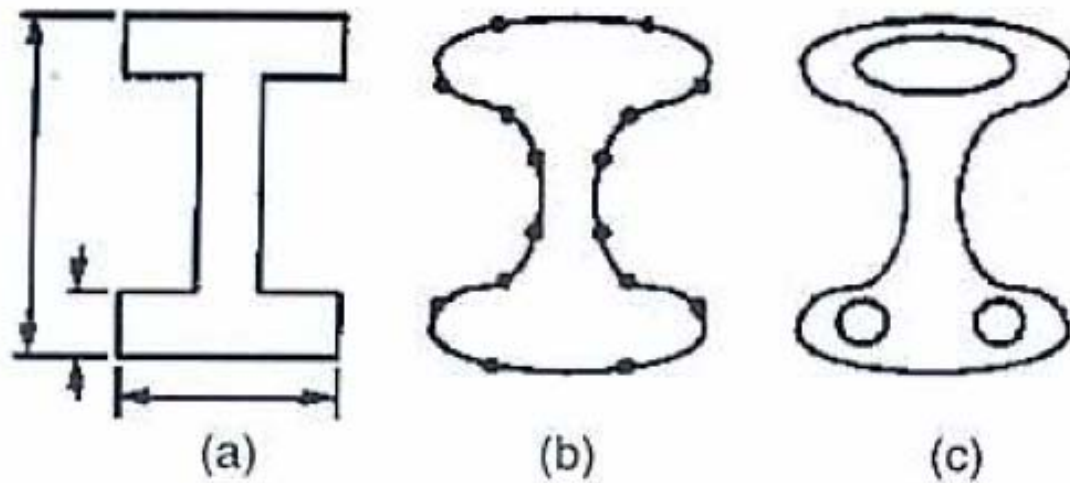


Figure 1.1 Types of geometry parameterization: (a) sizing, (b) shape, and (c) topology (Saitou *et al.*, 2005).

These three types of methods have been around for some time, but computing power has limited their use to research environments. The use of approximation methods provides a way to reduce the needed computational power making the use of optimization methods more practical in an industrial setting.

Approximation methods include surrogate modeling and reduced order modeling (Saitou *et al.*, 2005). The basic idea of surrogate modeling or metamodeling is to produce a function $z=f(x)$ that will accurately capture the response, z , with changes in the vector x . The function, $f(x)$, is not explicit; so, it is computationally less expensive but accurate

enough for the entire design space of the input variable x (Fang and Horstemeyer, 2006). The surrogate model method provides a quick and flexible way to conduct multi-objective design optimizations. The flexibility of this method allows for a variety of responses to be considered for optimization and allows for the optimization of a single part or a large system. Solanki *et al.*, (2007) used the surrogate method to reduce the weight of a control arm, and Fang *et al.*, (2004) used this method to simultaneously optimize multiple vehicle chassis components for crashworthiness. Reduced order model methods are also helpful in reducing computational expenses, but Fang *et al.*, (2005) explains that it is difficult to reproduce the constraints and loading conditions using this method and a reduced model can typically only consider one loading scenario. These limitations make reduce order modeling less attractive compared to the surrogate model method.

A great deal of work has been done in the area of multi-objective design optimization applied to structural design (Saitou *et al.*, 2005). Most of the work that has been conducted is based a von-Mises stress level component failure criteria. Horstemeyer (2001) showed that the area of highest von-Mises stress will not always be the location of the failure. By basing the failure criteria on von-Mises stress, the history of the material microstructure is not taken into account. An unsafe design can result by ignoring the history effects of the material. In order to insure a safe design, the history of the material along with the in-service life of the material must be taken into account. Fig 1.2 shows the typical manufacturing history and in-service life of a material. The internal state variable (ISV) damage material model considers the microstructural history of the

material. Horstemeyer and Wang (2003) explain how the ISV damage material model captures history effects by considering multiple length scales. Material characteristics on the nano, micro, and meso scales are evaluated and incorporated into the ISV model so that their effects can be seen on the macroscale (Bammann *et al.*, 1989). The ISV model is physically based and is consistent with continuum level kinetics, kinematics, and thermodynamics. The ISV damage model includes void nucleation, void growth, and void coalescence. This material model has been implemented into commercial finite element codes allowing for the microstructural material research to be incorporated into the FEA.

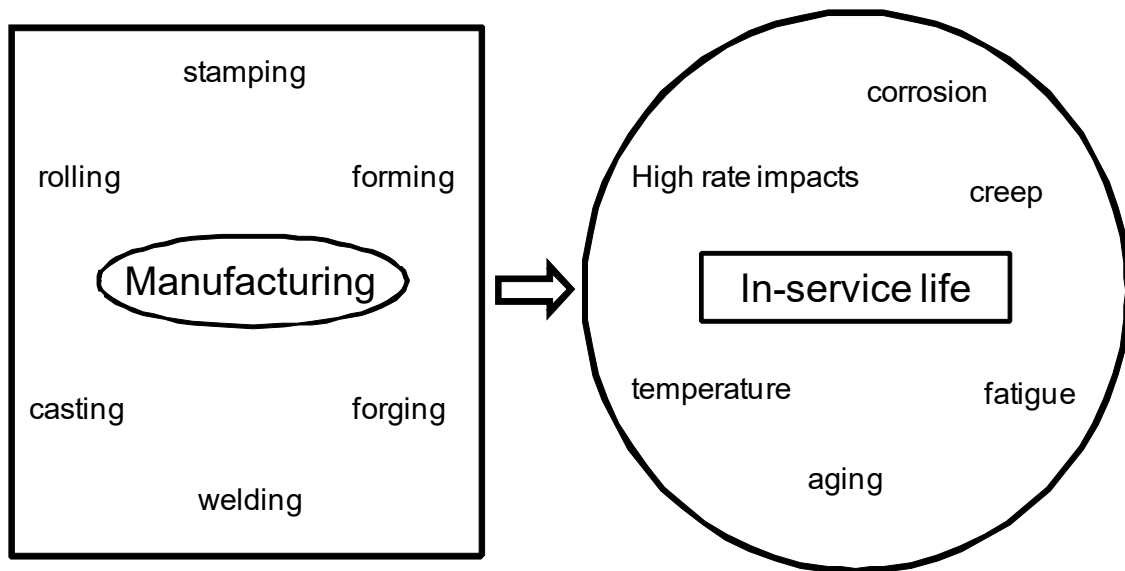


Figure 1.2. Typical manufacturing and in-service design scenarios (Horstemeyer and Wang, 2003).

By combining FEA, the ISV material model, and multi-objective design optimization, the designer has a powerful tool that will lead to far more advanced designs. This tool will allow the designer to meet more stringent design goals without drastically increasing product development time. The focus of this paper is to derive a road map for the implementation this design tool and to demonstrate its usefulness. The steps needed to use this tool will be discussed in-depth and two case studies of the multi-objective optimization will be discussed.

CHAPTER II

METAMODELING

In spite of advances in computing power, the computational cost of running high fidelity, complex engineering simulations make it impractical to rely exclusively on simulation codes for the purpose of design optimization (Jin, Chen and Simpson, 2001). One solution to this problem is the use of surrogate models or metamodels. These approximation models can be evaluated very quickly allowing for a reduction in computational cost. Metamodeling consists of approximating a true unknown function with a predefined function whose coefficients are to be determined by the true function values at some design points (Fang and Horstemeyer, 2006). Consider the function below:

$$y = f(\mathbf{x}) , \quad (2-1)$$

where $\mathbf{x} = [x_1, x_2, \dots, x_n]$ is a vector, n is the number of design variables, and y is the output. Look at the simple beam example given in Fig 2.1. The cross sectional geometry of the beam can be described in terms of design variables $\mathbf{x} = [x_1, x_2, \dots, x_4]$. P and Q are loads applied to the beam. Some responses of interest from a structural engineering stand point are: stress, displacement, natural frequency, and weight. These responses can be represented by the functions given below:

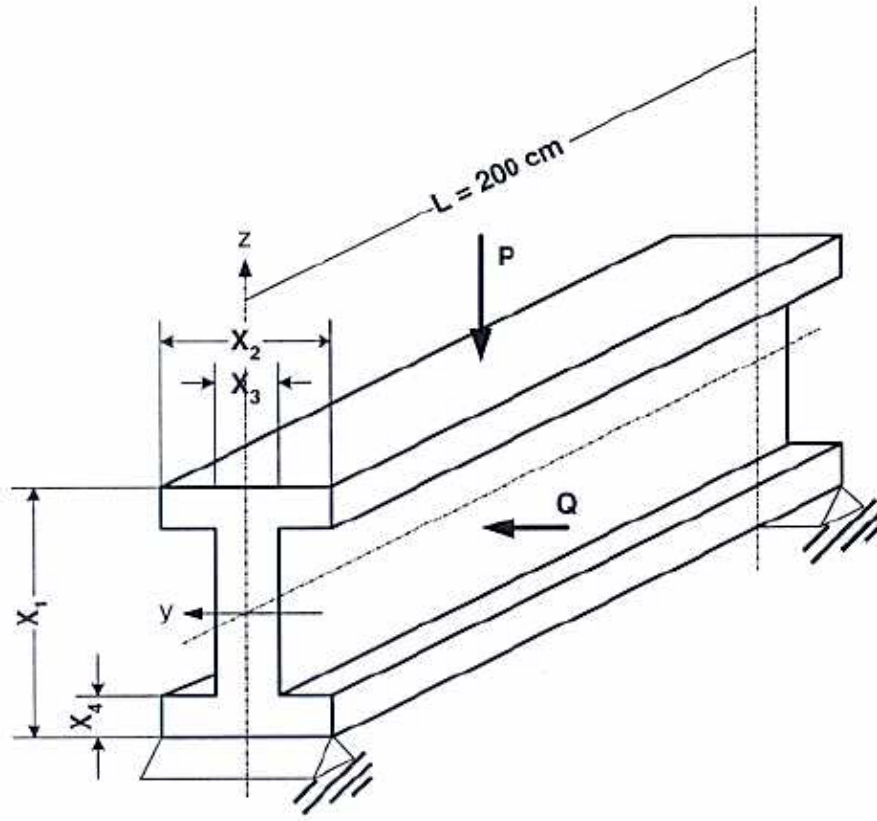


Figure 2.1. Beam example (Jin, Chen, and Simpson, 2002).

$$S = f(x_1, x_2, x_3, x_4), \quad (2-2)$$

$$D = g(x_1, x_2, x_3, x_4), \quad (2-3)$$

$$NF = h(x_1, x_2, x_3, x_4), \quad (2-4)$$

$$W = j(x_1, x_2, x_3, x_4), \quad (2-5)$$

where S is stress, D is displacement, NF is natural frequency, and W is weight. For most scientific and engineering applications it is desirable to obtain the explicit form of these functions, but the explicit form is usually unavailable or too costly to obtain. Therefore, these functions must be approximated. The approximation must be accurate enough to

represent the entire design space of the input variables (Fang and Horstemeyer, 2006), but light enough to avoid computational expenses. Fang, Rasi-Rohani, and Horstemeyer (2004) state that the basic idea of metamodeling is to construct an approximation model using function values at some sampling points, which are typically determined using design of experiments methods such as factorial design, central composite design, Latin Hypercube, or Taguchi orthogonal array.

There are many metamodeling techniques including: response surface methodology, Kriging, artificial neural network, multivariate adaptive regressive splines, local moving least square, Gaussian process, and radial basis functions (Jin, Chen, and Simpson, 2001), (Fang *et al.*, 2005), (Solanki *et al.*, 2007). Response surface methodology (RSM) has been predominately used for its simplicity and efficiency (Fang and Horstemeyer, 2006). The RSM uses quadric polynomials to develop an approximate model. The RSM formulation can be shown as:

$$f(x) = C_o + \sum_i C_i x_i + \sum_i C_{ii} x_i^2 + \sum_i \sum_j C_{ij} x_i x_j, \quad (2-6)$$

where C 's are the unknown coefficients. The unknown coefficients are determined using the method of least squares. To test the model fit to the true function, analysis variance can be used. Fang and Horstemeyer (2006) showed that the RSM could produce good approximations to some responses, but not for higher order, highly non-linear responses. Jin, Chen, and Simpson (2001) comment that the smoothing capability of polynomial regression allows for quick convergence of noisy functions, but instabilities may arise

when working with higher order polynomials or the number of required sample points may be too high.

Radial basis functions (RBF) use linear combinations of a radially symmetric function based on Euclidean distance (Jin, Chen, and Simpson, 2001). The RBF can be expressed as:

$$f(x) = \sum_i \lambda \phi(\|x - x_i\|), \quad (2-7)$$

where x is an input vector of design variables, λ is the basis function coefficient, and ϕ is the basis function. Fang, Solanki, and Horstemeyer (2005) demonstrated the accuracy of the RBF in full-scale vehicle crash simulations by successfully reducing intrusion distance while reducing vehicle mass. Fang and Horstemeyer (2006) compared RSM and RBF approximations showing that RBF approximations gave good results for both linear and highly non-linear responses. Fig 2.2 developed by Fang and Horstemeyer (2006) shows the RSM and RBF approximations along with the true functions. In Fig 2.2, RSM-LP refers to linear response surface methodology, RSM-QP refers to quadratic polynomial response surface methodology, and RBF-CS30-LP refers to radial basis function using a compactly supported basis function. Jin, Chen, and Simpson (2001) looked at the RBF as an approximation function for optimization purposes. They used fourteen different problems to compare RSM, RBF, Kriging, and multivariate adaptive regressive splines approximation methods. They reported that the RBF performed best in the categories of accuracy, robustness, and reduced sample size. One drawback to RBF approximations is that analysis of variance cannot be used. By nature, the RBF passes

through all the sampling points. To test the model fit, points other than the sampling points must be taken.

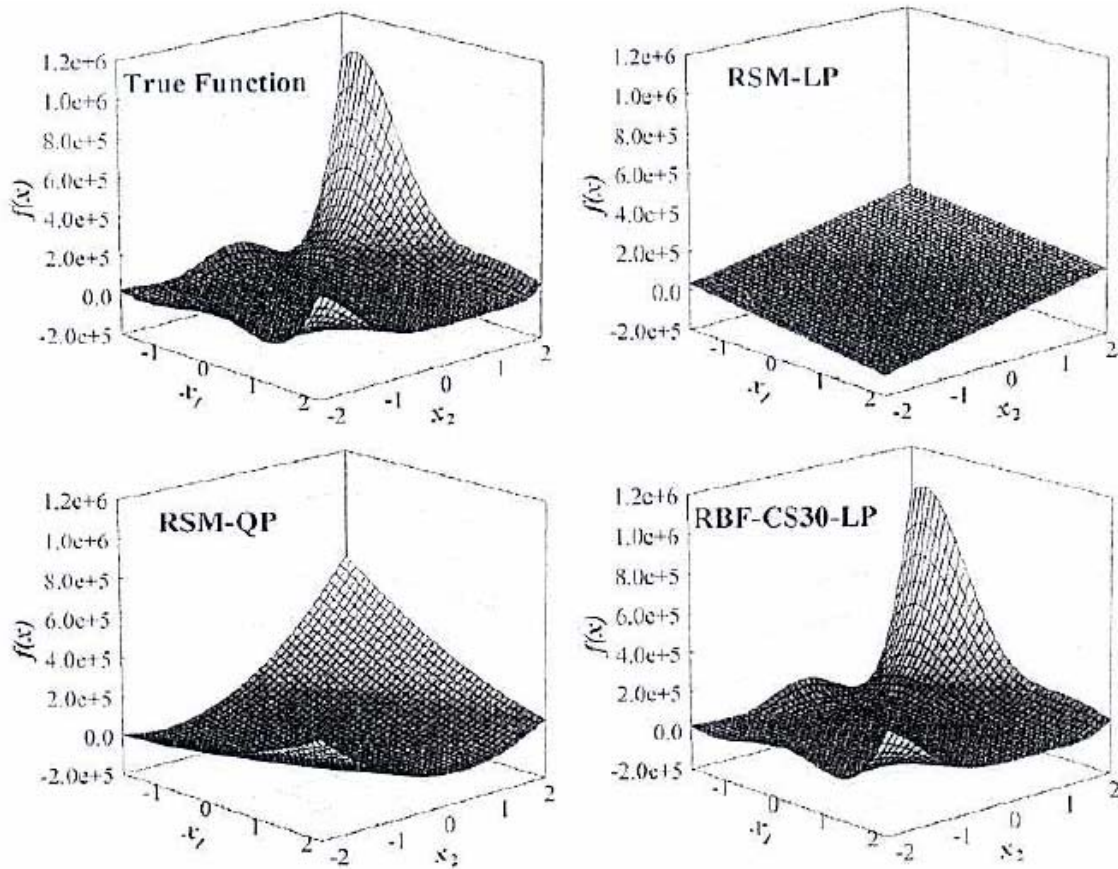


Figure 2.2. Comparison of the RSM and RBF models to the true function (Fang and Horstemeyer, 2006).

For the case studies in this paper, RBF metamodel approximations will be used. RBF were selected based on their proven success in multi-objective design optimization problems. Also, the demonstration of RBF to produce accurate results given small sample size makes them very attractive for optimization problems. HIPPO (Fang and

Horstemeyer, 2004) is a design optimization program developed at the Center for Advanced Vehicular Systems. HIPPO will produce RBF using a variety of different basis functions. There have been other routines developed in MATLAB (MathWorks 2007) and Excel that will also quickly and conveniently produce metamodels of varying formulations (Solanki *et al.*, 2007), (Gu, Li, and Yang, 2004). HIPPO and MATLAB will be used for the generation of metamodels for the optimizations performed in this study.

CHAPTER III

MATERIAL MODEL

Introduction

The internal state variable material model is thermodynamically constrained and is physically based upon microstructure property relations (Horstemeyer and Wang, 2003). An ISV plasticity model was presented by Bammann *et al.* (1989) and later was modified by Horstemeyer and Gokale (1999) to include damage nucleation, growth, and coalescence. The ISV plasticity-damage model has been used to model many metals such as steel, aluminum, titanium, and magnesium. The Aluminum 6061 material constants used in this study were correlated by Agarwal *et al.* (2001). The ISV model has been implemented in several finite element codes including: DYNA2D, DYNA3D, PRONTO2D, PRONTO3D, JAC3D, ABAQUS, and NIKE2D (Bammann *et al.*, 1993). The ISV model allows for a design team comprised of a designer, material scientist and finite element analyst to be reduced to a single person. The ISV model is a physically based plasticity damage model that includes microstructural content and is consistent with continuum level kinetics, kinematics and thermodynamics. The ISV model is a design tool that allows the microstructure analysis to be combined with the finite element analysis (cf. Horstemeyer and Wang, 2003). This design tool helps to streamline the design process.

Plasticity Model Formulation

The plasticity model formulation is shown in this section; however, the formulation of this model is discussed with more detail by Bammann *et al.* (1993), Horstemeyer *et al.*, (2000), and Horstemeyer (2001). The kinematics of the plasticity model are based on the decomposition of the of the deformation gradient into elastic, deviatoric plastic, and dilatational plastic parts (Bammann *et al.* 1993). It is important to note that any second order tensor variable \underline{X} , $\dot{\underline{X}}$ represents an objective rate, and for any scalar variable X , \dot{X} represents a time rate of change. The symmetric and skew symmetric parts of velocity gradient are decomposed into elastic and plastic parts \underline{D} and \underline{W} . The rate of deformation is the symmetric tensor and is defined as

$$\underline{D} = \underline{D}^e + \underline{D}^p + \underline{D}^v \quad (3-1)$$

and can also be written as

$$\underline{D}^e = \underline{D} - \underline{D}^{in}, \quad (3-2)$$

where \underline{D} represents the total deformation, \underline{D}^e is the elastic part, \underline{D}^p is the deviatoric plastic, \underline{D}^v is the plastic volumetric part, and \underline{D}^{in} is the deviatoric inelastic flow rule.

The spin tensor is the skew symmetric tensor and is defined as

$$\underline{W} = \underline{W}^e + \underline{W}^p, \quad (3-3)$$

where \underline{W}^e is the plastic part and \underline{W}^p is the deviatoric plastic part. It is important to note that the volumetric spin, \underline{W}^v , is assumed to be zero.

Assuming linear isotropic elasticity with respect to natural configuration, linear elasticity can be written in the form of

$$\dot{\underline{\sigma}} = \dot{\underline{\sigma}} - \underline{W}^e \underline{\sigma} - \underline{\sigma} \underline{W}^e = \lambda (1 - D) \text{tr}(\underline{D}^e) \underline{I} + 2\mu (1 - D) \underline{D}^e - \frac{\dot{D}}{1 - D} \underline{\sigma}. \quad (3-4)$$

The Cauchy stress is $\underline{\sigma}$, the elastic spin is \underline{W}^e , and λ and μ are the elastic Lamé constants. The yield function is used to determine whether the state of stress is elastic or plastic. The deviatoric inelastic flow rule, \underline{D}^{in} , is employed if the state of stress is plastic. The deviatoric inelastic flow rule (Equation 3-5) accounts for creep and plasticity and is a function of temperature, kinematic hardening internal state variable ($\underline{\alpha}$), the isotropic internal state variable (R), and the temperature dependent functions $f(T)$, $Y(T)$, and $V(T)$. The three functions $f(T)$, $Y(T)$, and $V(T)$ determine the yield stress and are given in Equations (3-6), (3-7) and (3-8), respectively. $Y(T)$ is the rate independent yield stress, where $V(T)$ is the rate dependent yield stress. The function $f(T)$ determines the point when strain rate affects yielding.

$$\underline{D}^{in} = f(T) \sinh \left[\frac{\|\underline{\sigma}' - \underline{\alpha}\| - \{R + Y(T)\} \{1 - D\}}{V(T) \{1 - D\}} \right] \frac{\underline{\sigma}' - \underline{\alpha}}{\|\underline{\sigma}' - \underline{\alpha}\|} \quad (3-5)$$

$$f(T) = C_3 \exp\left(-C_4/T\right), \quad (3-6)$$

$$Y(T) = C_1 \exp\left(-C_2/T\right), \quad (3-7)$$

$$V(T) = C_5 \exp\left(-C_6/T\right), \quad (3-8)$$

The constants C_1 thru C_6 are determined by compression test conducted at varying temperatures and strain rates.

The kinematic hardening internal state variable (α) and the isotropic hardening internal state variable (R) reflect the effect of anisotropic dislocation density and the effects of the global dislocation density respectively and are given in Equations (3-9) and (3-10). The kinematic hardening and recovery describes the effects of local dislocation interaction with barriers and affects the yield locally. The isotropic hardening accounts for the effects of dislocations on the global scale and results in a uniform growth of the yield stress. The kinematic and isotropic hardening equations are given by

$$\dot{\alpha} = \left\{ h(T) \underline{D}^p - \left[\sqrt{\frac{2}{3}} r_d(T) \|\underline{D}^p\| + r_s(T) \right] \|\alpha\| \alpha \right\} \left(\frac{GS_0}{GS} \right)^Z, \quad (3-9)$$

$$\dot{R} = \left\{ H(T) \|\underline{D}^p\| - \left[R_d(T) \|\underline{D}^p\| + R_s(T) \right] R^2 \right\} \left(\frac{GS_0}{GS} \right)^Z. \quad (3-10)$$

The function $h(T)$ is the anisotropic hardening modulus, and $H(T)$ is the isotropic hardening modulus. The functions $r_d(T)$ and $R_d(T)$ are scalar functions describing the describing the dynamic recovery. The scalar functions $r_s(T)$ and $R_s(T)$ describe diffusion-controlled static or thermal recovery. These functions are

$$r_d(T) = C_7 \left(1 + C_{19} \left[\frac{4}{27} - \frac{J_3'^2}{J_2'^3} \right] \right) \exp\left(-C_8/T\right), \quad (3-11)$$

$$h(T) = \left\{ C_9 \left(1 + C_{20} \left[\frac{4}{27} - \frac{J_3'^2}{J_2'^3} \right] \right) \right\} - C_{10}T, \quad (3-12)$$

$$r_s(T) = C_{11} \exp\left(-C_{12}/T\right), \quad (3-13)$$

$$R_d(T) = C_{13} \left(1 + C_{21} \left[\frac{4}{27} - \frac{J_3'^2}{J_2'^3}\right]\right) \exp\left(-C_{14}/T\right), \quad (3-14)$$

$$H(T) = \left\{ C_{15} \left(1 + C_{22} \left[\frac{4}{27} - \frac{J_3'^2}{J_2'^3}\right]\right) \right\} - C_{16}T, \quad (3-15)$$

$$R_s(T) = C_{17} \exp\left(-C_{18}/T\right), \quad (3-16)$$

where $J_2' = \frac{1}{2}(\underline{\sigma}' - \underline{\alpha})^2$ and $J_3' = \frac{1}{3}(\underline{\sigma}' - \underline{\alpha})^3$. The deviatoric stress $\underline{\sigma}'$ is expressed in

indicial notation as $\sigma_{ij}' = \sigma_{ij} - \frac{1}{3}\sigma_{ii}$. The constants C_7 to C_{22} are material constants that

are determined by compression test at varying strain rates and temperatures.

Damage Model Formulation

Damage in ductile metals is the result of void nucleation, growth, and coalescence. Fig 3.1 shows examples of void nucleation, growth, and coalescence separately, but realistically these occur simultaneously. Void nucleation is the formation of new voids in the material, void growth is the increase in size of newly formed and existing voids, and void coalescence is the interaction of voids that ultimately results in a fracture path and macroscopic failure. Simultaneous void growth and nucleation is shown in Fig 3.2. In Fig 3.2, a second phase particle that has separated from the matrix, and a void has formed. The void continues to grow, and new voids form at neighboring

particles. Eventually, the voids will grow large enough that they interact and coalesce. This example lays out the considerations of the damage material model. The ISV damage model laid out by Horstemeyer *et al.*, (2000) and Hammi, Hostemeyer, and Bammann (2003) considers simultaneous void nucleation, growth and coalescence in its formulation. The model accounts for void nucleation by second phase particle decohesion and particle fracture. The model allows for void growth at multiple locations around the void. The development of the damage formulation is discussed in-depth in Horstemeyer and Gokhale (1999), Horstemeyer et al., (2000), and Horstemeyer (2001). The damage, ϕ , is defined as the change in the ratio of the volume of an element in the elastically unloaded state from the initial reference state and is written in the form of

$$\phi = \frac{V_v}{V_2} = \frac{V_v}{N} \frac{N}{V_2} = v_v \eta, \quad (3-17)$$

where

$$V_v = \eta^* V_o v_v, \quad (3-18)$$

$$V_2 = V_o - V_v, \quad (3-19)$$

$$\eta^* = N / V_o. \quad (3-20)$$

N is the total number of voids in the continuum volume, and v_v is the average void volume from each particle that has nucleated a void.

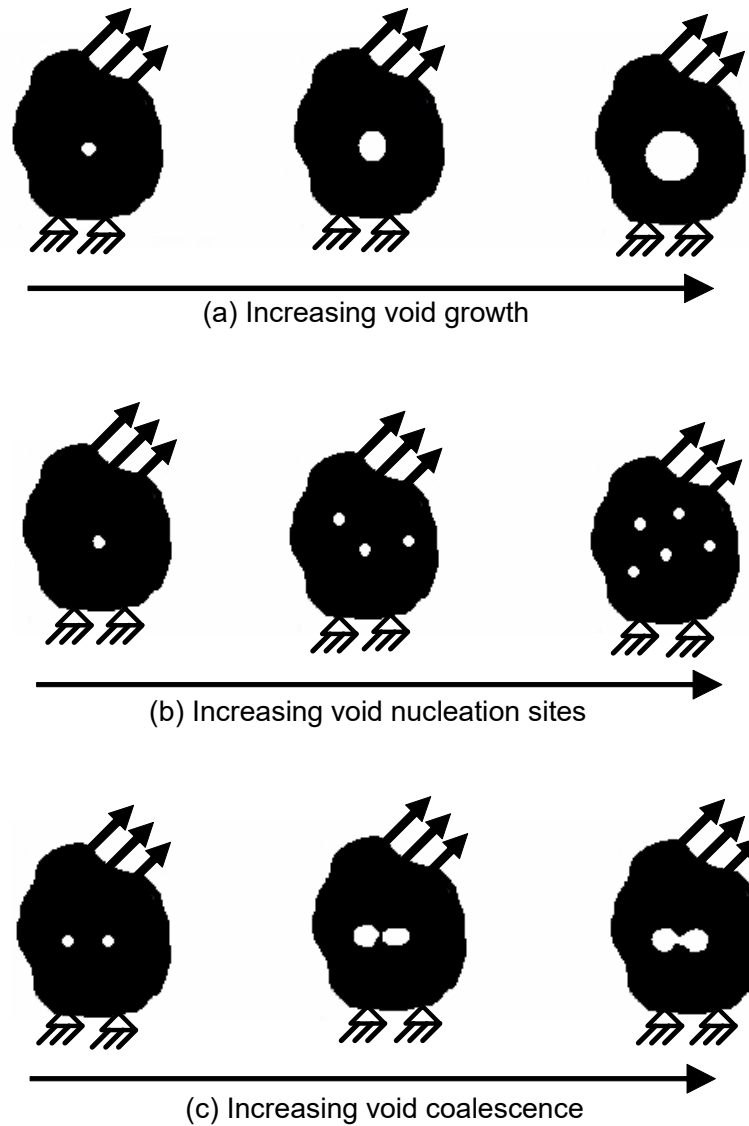


Figure 3.1. Schematic of the fictitious material with (a) increasing void nucleation (b) increasing void growth and (c) occurrence of void coalescence (Horstemeyer *et al.*, 2000).

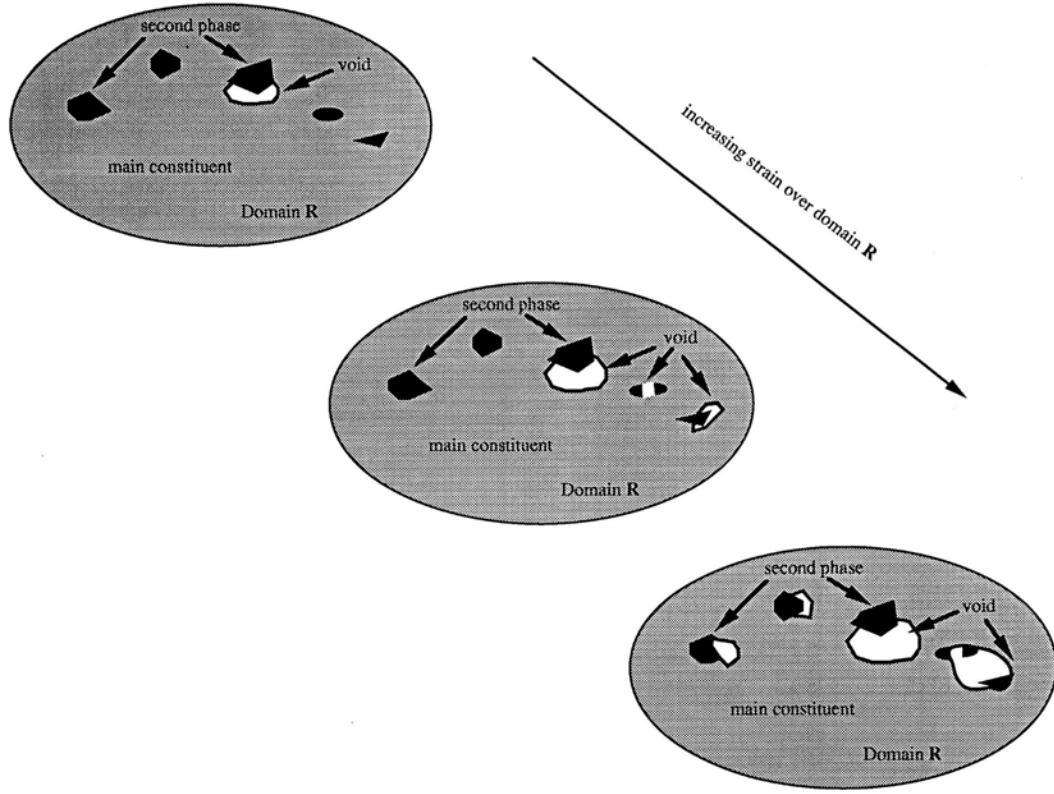


Figure 3.2. Schematic of the fictitious material with increasing nucleation density and void growth of a model framework (Horstemeyer, 2000)

The void nucleation rule used in the model follows the work done by Horstemeyer and Gohkale (1999). The void nucleation function in the integrated form is given by,

$$\eta(t) = C_{coeff} \exp \left(\frac{\varepsilon(t)d^{1/2}}{K_{IC}f^{1/3}} \left\{ a \left[\frac{4}{27} - \frac{J_3^2}{J_2^3} \right] + b \frac{J_3}{J_2^{3/2}} + c \left\| \frac{I_1}{\sqrt{J_2}} \right\| \right\} \right) \exp \left(\frac{C_{\eta T}}{T} \right), \quad (3-21)$$

where C_{coeff} is a material constant, $\varepsilon(t)$ is the strain rate, $C_{\eta T}$ is a temperature dependent material constant, and T is temperature. The volume fraction of the second phase particles is captured by the f constant, d is the average size of the second phase particle,

and K_{IC} is the fracture toughness. The model constants a , b , and c capture the effect of void fraction resulting from local microstresses. These constants are determined from uniaxial tension, compression, and torsion experiments where the number of nucleation sites is counted using various microscopy techniques. The rate at which voids nucleate is dependent on the stress state: tension, compression, and torsion. Horstemeyer and Gokhale (1999) account for the stress state dependency in the damage model by using deviatoric stress invariants:

$$I_1 = \sigma_{kk} \quad (3-22)$$

$$J_2 = \frac{1}{2} S_{ij} S_{ij} \quad (3-23)$$

$$J_3 = S_{ik} S_{ij} S_{ki} \quad (3-24)$$

$$S_{ij} = \sigma_{ij} - \frac{1}{3} \delta_{ij} \sigma_{kk}. \quad (3-25)$$

The damage model uses the void growth rule developed by Cocks and Ashby (1980) for the growth of large voids. The void growth rule is the void volume fraction rate equation and is highly dependent on stress triaxiality. The void growth rule is

$$\dot{\phi}_{pores} = 1 - \left[1 + \left[\left(1 - \phi_{pores} \right)^{1 + \frac{V(T)}{Y(T)}} - 1 \right] \exp \beta \chi \varepsilon(t) \left(1 + \frac{V(T)}{Y(T)} \right) \right]^{\frac{1}{1 + \frac{V(T)}{Y(T)}}}, \quad (3-26)$$

where

$$\chi = \frac{\sigma_H}{\sigma_{vm}}, \quad (3-27)$$

σ_H is the hydrostatic stress, σ_{vm} is the von Mises stress, and ϕ_{pore} is related to the initial porosity.

The model uses the void growth rule of McClintock (1968) for growth of smaller, newly formed voids. These are voids that have just nucleated. The void growth rule developed by McClintock (1968) is

$$v = \frac{4}{3} \left[R_0 \exp \left(\varepsilon(t) \frac{\sqrt{3}}{2(1-n)} \times \sinh \left(\sqrt{3}(1-n) \frac{\sqrt{2}I_1}{3\sqrt{J_2}} \right) \right) \right]^3, \quad (3-28)$$

where R_0 is the initial radius of the voids and n is strain hardening constant.

The coalescence rule is given in Equation (3-29). This coalescence formulation accounts for the influence of nearby voids on each other and growth of two voids into one.

$$C = [C_{D1} + C_{D2} \eta v \left(\frac{GS_0}{GS} \right)^Z] (C_{CT} T), \quad (3-29)$$

where h is the void nucleation rule given in Equation (3-21) and n is the small void growth rule given in Equation (3-28). The constant C_{D1} relates to the simple case where two voids grow together and become one and C_{D2} relates the second case where smaller voids nucleation and growth are influenced by nearby larger voids nucleating and growing. The C_{CT} parameter is a material constant. The constants C_{D1} , C_{D2} , and C_{CT} must be determined experimentally.

The total damage accounts for void nucleation, void growth, and void coalescence. The total damage equation is composed of Equations (3-21), (3-26), (3-28), and (3-29) and is shown as

$$\phi = C(\eta\nu + \phi_{pore}) \quad (3-30)$$

The rate formulation of the damage equations in terms of the observable and state variables and are given in Equation 3-31 through 3-36:

$$\dot{D} = [\dot{\phi}_{particles} + \dot{\phi}_{pores}] C + [\phi_{particles} + \phi_{pores}] \dot{C} \quad (3-31)$$

$$\dot{\phi}_{particles} = \dot{\eta}\nu + \eta\dot{\nu} \quad (3-32)$$

$$\dot{\eta} = \left\| \underline{D}^P \right\| \frac{d^{1/2}}{K_{IC} f^{1/3}} \eta \left\{ a \left[\frac{4}{27} - \frac{J_3^2}{J_2^3} \right] + b \frac{J_3}{J_2^{3/2}} + c \left\| \frac{I_1}{\sqrt{J_2}} \right\| \right\} \exp\left(\frac{C_{nT}}{T} \right) \quad (3-33)$$

$$\dot{\nu} = \frac{\sqrt{3}R_0}{2(1-n)} \left[\sinh \left(\sqrt{3}(1-n) \frac{\sqrt{2}I_1}{3\sqrt{J_2}} \right) \right] \left\| \underline{D}^P \right\| \quad (3-34)$$

$$\dot{\phi}_{pores} = \left[\frac{1}{(1-\phi_{pores})^m} - (1-\phi_{pores}) \right] \sinh \left\{ \frac{2 \left(2^{V(T)/Y(T)} - 1 \right) \sigma_H}{\left(2^{V(T)/Y(T)} + 1 \right) \sigma_{vm}} \right\} \left\| \underline{D}^P \right\| \quad (3-35)$$

$$\dot{C} = C_{coal} [\eta\dot{\nu} + \dot{\eta}\nu] \exp(C_{CT}T) \left(\frac{GS_0}{GS} \right)^Z \quad (3-36)$$

Numerical Implementation

The ISV damage material model has been implemented in to several commercial finite element codes such as: DYNA2D, DYNA3D, PRONTO2D, PRONTO3D, JAC3D, ABAQUS, and NIKE2D (Bammann *et al.*, 1993). The implementation is discussed in great detail in Bammann *et al.*, (1993), Horstemeyer *et al.*, (2000), and Horstemeyer (2001). The solver in a finite element code uses an operator split. The operator split ensures that equilibrium is maintained by assuming that the stress state is constant over the time step. This results in the determination of the velocity gradient. At the end of each time step, the stress state is updated. To implement the damage model, a second operator split is defined. In the second operator split, the damage is assumed constant when the stress is updated. After the new stress is applied, the damage is updated to the new level based on the updated stress and velocity gradient. The time steps will continue as stated until the simulation is complete or the damage value reaches 1. The element has failed at the damage level of 1. For engineering purposes the material would most likely be considered failed at a much lower damage level of around 50% or less (Horstemeyer, 2001). This is due to the highly degraded elastic moduli. Horstemeyer (2001) states that the damage level approaches unity very rapidly after reaching 50% due to the nature of the void growth rule.

The first step to implementing the ISV damage model is to rewrite the hardening rate equations (Equations 3-9 and Equations 3-10) by replacing the deviatoric plastic rate of deformation with the total rate of deformation. The new hardening rate equations are

$$\dot{\underline{\alpha}} = h(T)\underline{D}_d^p - [r_d(T)\sqrt{\frac{2}{3}}\|\underline{D}\| + r_s(T)]\sqrt{\frac{2}{3}}\|\underline{\alpha}\|\underline{\alpha} \quad (3-38)$$

$$\dot{R} = \sqrt{\frac{2}{3}}H(T)\|D_d^p\| - [R_d(T)\sqrt{\frac{2}{3}}\|\underline{D}\| + R_s(T)]R|R. \quad (3-39)$$

Next, the radial return method is used to give trial values for the deviatoric stress and the internal hardening variables. This is accomplished by assume the strain to be purely elastic or $\underline{D}_d^p = 0$ (Horstemeyer, 2001). Horstemeyer (2001) used the schematic in Fig 3-3 to demonstrate the radial return method. The deviatoric stress and internal hardening equations are given in Equations (3-40) thru (3-42) where N represents the value of the time step and N+1 represents the value of time step at N+1.

$$\underline{\sigma}_{N+1}^{trial} = \underline{\sigma}'_N + \int_{t_N}^{t_{N+1}} 2\mu(1-\phi)\underline{D}' dt - \int_{t_N}^{t_{N+1}} \frac{\dot{\phi}\underline{\sigma}'}{1+\phi} dt \approx \underline{\sigma}'_N \left(1 - \frac{\phi\Delta t}{1+\phi}\right) + 2\mu(1-\phi)\underline{D}' \Delta t \quad (3-40)$$

$$\underline{\alpha}_{N+1}^{trial} = \underline{\alpha}_N + \int_{t_N}^{t_{N+1}} (r_d\sqrt{\frac{2}{3}}\|\underline{D}\| + r_s)\sqrt{\frac{2}{3}}\|\underline{\alpha}\|\underline{\alpha} dt \approx \{1 - (r_d\sqrt{\frac{2}{3}}\|\underline{D}\| + r_s)\sqrt{\frac{2}{3}}\|\underline{\alpha}\|\Delta t\}\underline{\alpha}_N \quad (3-41)$$

$$R_{N+1}^{trial} = R_N + \int_{t_N}^{t_{N+1}} (R_d\sqrt{\frac{2}{3}}\|\underline{D}\| + R_s)|R|R \approx \{1 - (R_d\sqrt{\frac{2}{3}}\|\underline{D}\| + R_s)\sqrt{\frac{2}{3}}|R|R\Delta t\}R_N \quad (3-42)$$

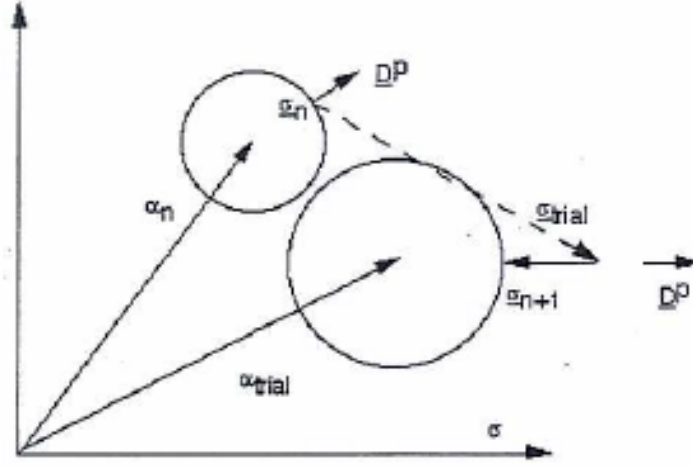


Figure 3.3. Radial return algorithm used to update new state as predicted by model (Horstemeyer, 2001).

Next, the tensor $\underline{\xi} = \underline{\sigma}^{trial} - \frac{2}{3}\underline{\alpha}$ is used to redefine the flow rule as

$$\underline{D}_d^p = \sqrt{\frac{2}{3}} f(T) \sinh \left(\frac{\sqrt{\frac{3}{2}} \|\underline{\xi}\| - (R - Y(T)(1 - \phi))}{V(T)(1 - \phi)} \right) \frac{\underline{\xi}}{\|\underline{\xi}\|} \quad (3-43)$$

Then, the norm is taken of both sides of the flow rule, and it is inverted to yield:

$$\Phi = \sqrt{\frac{3}{2}} \|\underline{\xi}\| - (1 - \Phi) [R + Y + V \sinh^{-1} \left(\frac{\sqrt{\frac{2}{3}} \|\underline{D}_d^p\|}{f} \right)] = 0 \quad (3-44)$$

This form of the flow equation is then evaluated. Bammann *et al.* (1993) states that if $\Phi^{trial} \leq 0$, the elastic assumption is valid and the trial values of $\underline{\sigma}$, $\underline{\alpha}$, and \underline{R} can be used.

If not, corrections must be made to the trial values and these corrected terms are:

$$\sigma'_{N+1} = \sigma_{N+1}^{trial} + \int_{t_N}^{t_{N+1}} 2\mu(1 - \phi) D^p dt = \sigma_{N+1}^{trial} - \frac{2\mu(1 - \phi)\gamma}{\|\underline{\xi}\|} \underline{\xi} \quad (3-45)$$

$$\underline{\alpha}_{N+1} = \underline{\alpha}_{N+1}^{trial} + \int_{t_N}^{t_{N+1}} h(T) D^P dt = \underline{\alpha}_{N+1}^{trial} + \frac{h\gamma}{\|\xi\|} \xi \quad (3-46)$$

$$R_{N+1} = R_{N+1}^{trial} + \sqrt{\frac{2}{3}} \int_{t_N}^{t_{N+1}} H(T) \|D^P\| dt = R_{N+1}^{trial} + \sqrt{\frac{2}{3}} H\gamma \quad (3-47)$$

where $\int_{t_n}^{t_{n+1}} D^P dt = \frac{\gamma}{\|\xi\|} \xi$ and $\int_{t_n}^{t_{n+1}} \|D^P\| dt = \gamma$.

The updated trial values are then substituted back into the inverted flow rule. Solving for γ so that $\Phi = 0$, gives

$$\gamma = \frac{\|\xi\| - \sqrt{\frac{2}{3}} (1 - \phi) (Y + R + V \sinh^{-1}(\frac{\|D\|}{f}))}{2\mu(1 - \phi) + \frac{2}{3} (h + H(1 - \phi))} \quad (3-48)$$

Now, the total effective strain is calculated and given by

$$\varepsilon_{N+1} = \varepsilon_N + \sqrt{\frac{2}{3}} \gamma, \quad (3-49)$$

and J_2 and J_3 are updated to calculate the new damage which leads to the new damage equations:

$$\eta_{N+1} = C_{coeff} \exp\left(\frac{\varepsilon_{N+1} d^{1/2}}{K_{IC} f^{1/3}} \left\{ a \left[\frac{4}{27} - \frac{J_3^2}{J_2^3} \right] + b \frac{J_3}{J_2^{3/2}} + c \left\| \frac{I_1}{\sqrt{J_2}} \right\| \right\}\right) \exp\left(\frac{C_{\eta T}}{T}\right) \quad (3-50)$$

$$\phi_{pores\ N+1} = 1 - \left[1 + \left[(1 - \phi_{pores})^{1 + \frac{V(T)}{Y(T)}} - 1 \right] \exp \beta \chi \varepsilon_{N+1} \left(1 + \frac{V(T)}{Y(T)} \right) \right]^{1 + \frac{V(T)}{Y(T)}} \quad (3-51)$$

$$v_{N+1} = \frac{4}{3} \pi \left[\varepsilon_{N+1} \sqrt{\frac{3}{2(1-n)}} \sinh \left(\sqrt{3}(1-n) \frac{\sqrt{2} I_1}{3\sqrt{J_2}} \right) \right]^3 \quad (3-52)$$

$$C_{N+1} = [C_{D1} + C_{D2}\eta_{N+1}v_{N+1}] \left(\frac{GS_0}{GS} \right)^z (C_{CT}T) \quad (3-53)$$

$$\phi_{N+1} = (\eta_{N+1}v_{N+1} + \phi_{pore\ N+1}) C_{N+1} \quad (3-54)$$

Equations (3-50) thru (3-54) originated from Equation (3-21), Equation (3-26), Equation (3-28), and Equation (3-29).

Finally, the pressure is calculate as

$$p_{N+1} = \frac{1}{3} tr(\sigma_n)(1 - \varphi) + (1 - \varphi)\Delta t K tr(D), \quad (3-55)$$

and the total stress is updated for that time step.

$$\sigma_{N+1} = \sigma'_{N+1} + p_{N+1} \quad (3-56)$$

This process is repeated for each time step until the full increment is complete.

CHAPTER IV

MULTI-OBJECTIVE DESIGN OPTIMIZATION PROCESS

Introduction

In order for designers to meet today's demands for safer and lighter products, a design tool is needed that can produce the optimum design without increasing the product development time. FEA has traditionally been used to conduct design optimization, but the traditional simulation based optimization is an iterative process that is heavily reliant on a human interaction and human judgment. Fig 4.1 lays out the simulation based optimization process. The designer starts with an initial design and performs a finite element simulation on the design. The designer views the results, and based on these results the designer makes changes to the initial design. Once the changes are made, another simulation is conducted on the newly modified part. This circular process continues until the engineer is satisfied that the optimal design has been achieved and error has been reduced. Simulation based design optimization has been used with success. Products that are statically loaded and are not exposed to multiple load cases could easily be optimized using the simulation based process, but in cases where a part will be exposed to many different load cases it becomes impossible to use this process successfully.

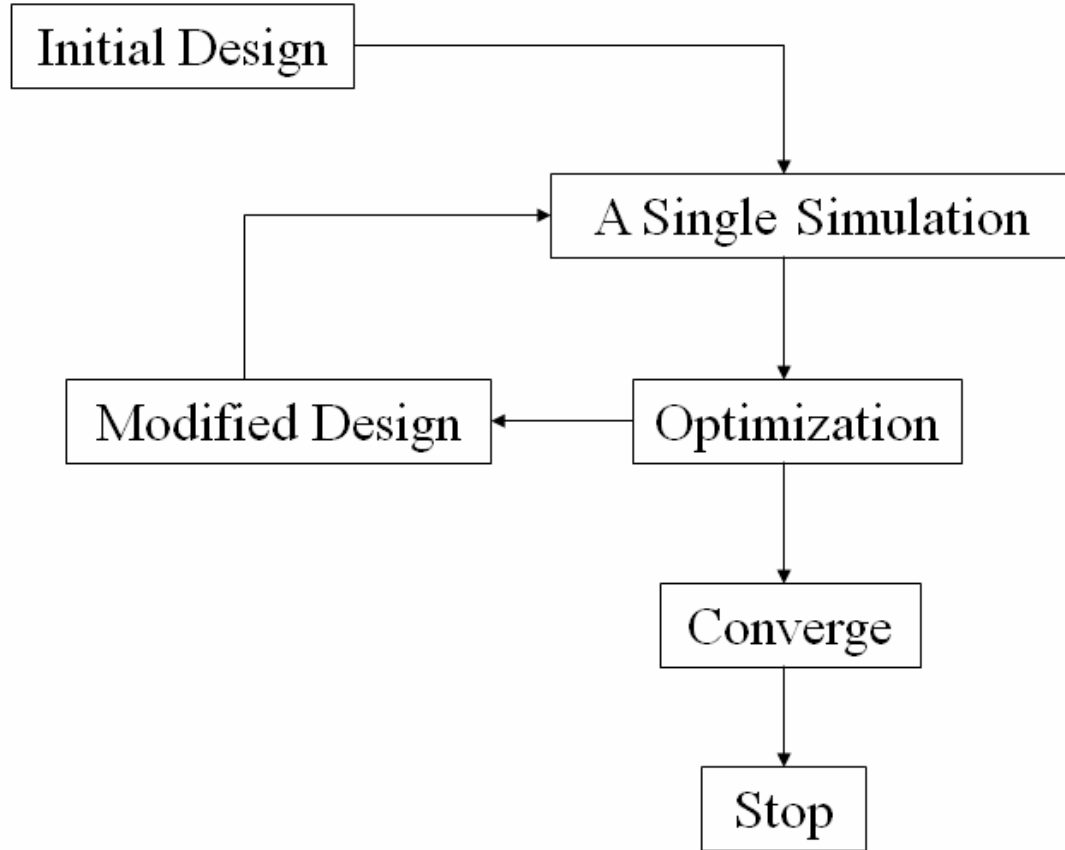


Figure 4.1. Simulation based design optimization process flowchart.

Consider a control arm from an automobile. During the control arm's life time it will be loaded in many ways. A few load cases might be: a pothole strike, a driver suddenly applying the brakes, and a high speed turn. Each of these load scenarios places forces of different magnitude and direction on the control arm. So, each load case could produce a peak stress at different locations on the control arm. Making a design change at one location of the control arm could reduce the stress in one load case while increasing it in another. On top of considering stress in each load case, the designer must consider other

responses such as modal frequency, stiffness, and weight. This is too much information to process, and an optimal design will never be found using a single objective simulation based optimization. On the other hand, multi-objective design optimization can consider all the load cases and design objectives in order to find a true optimum design.

Multi-objective design optimization eliminates the need for human interaction and judgment during the optimization. Fig 4.2 shows the flow of the multi-objective design optimization. There is no iterative process. Each of the load scenarios is considered in parallel during the optimization step, and a true optimal design is obtained. In cases such as the control arm or complex assemblies, a multi-objective optimization routine can eliminate the guessing game conducted by the designer and achieve the design requirements.

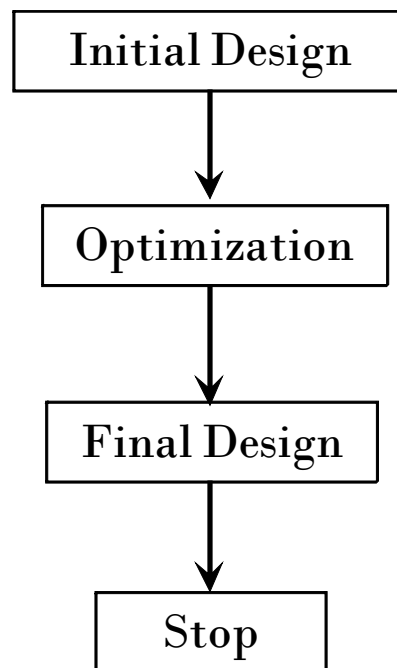


Figure 4.2. Multi-objective design optimization flow chart.

Process

This section will layout the steps to the multi-objective design process in detail. The type of optimization here focuses on size and utilizes metamodeling. Size optimization provides an effective method for improving current designs and can easily be implemented into the metamodeling approach. Metamodeling provides a means to reduce optimization time and provides a great deal of flexibility when defining the objectives and constraints.

The first step in the optimization process is to select the design variables. The design variables describe the geometry of the part or system to be optimized. Fig 4.3 shows a beam. It is desired to optimize the cross-section of the beam. Design variables are selected so that the cross section of the beam can be altered by changing the design variables. Some care should be taken when selecting the design variables. Notice that the length of the beam is fixed and not included as a design variable. This provides a way to set constraints on the geometry. Just as the length of the beam is fixed, features that are required to maintain the functionality of a part can be fixed by careful selection of the design variables. A few such features include: mounting holes, bearing pockets, retaining groves, etc. The number of design variables selected is also an important factor. Too many design variables will increase the problem size and computing time. If too few are selected, the desired objectives may not be achievable.

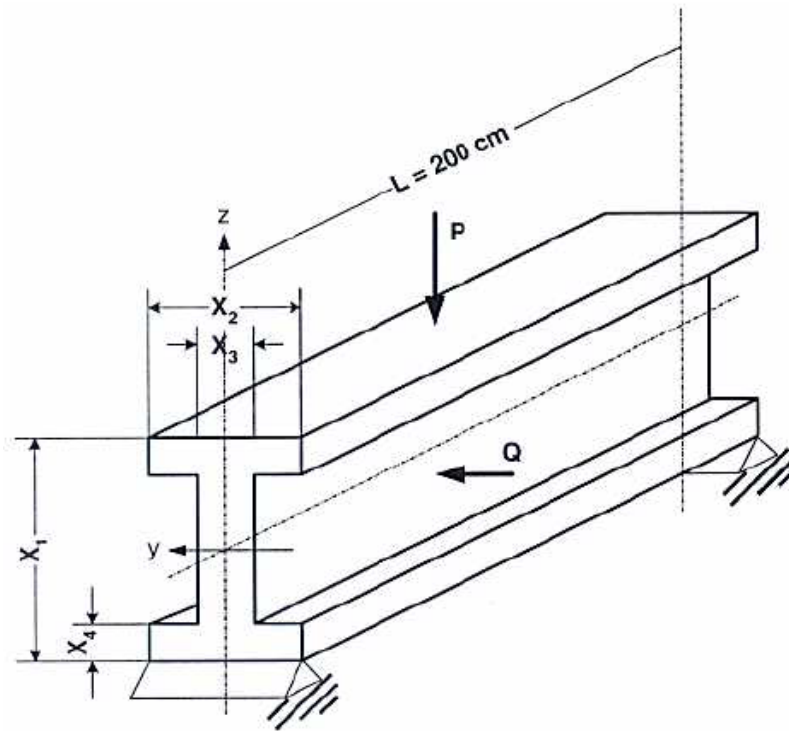


Figure 4.3. Beam example (Jin, Chen, and Simpson, 2002).

Once the number of design variables is known, the design of experiments (DOE) can be selected. There are a number of DOE to choose from: full factorial, Taguchi orthogonal array, central composite design, and Latin hypercube sampling to name a few. The DOE is another area that requires some attention. The DOE provides the sampling points used to create the metamodels. More sampling points generally provide a better fits. A full factorial will provide the best results but at the cost of the most required simulations. For example, a problem with 12 design variables with three levels would require 1728 models where a Taguchi orthogonal array would only require 27 models. For this reason, it is usually desired to sacrifice accuracy to save computation time. Fig 4.4 shows a DOE with four design variables and nine models. Each row of the matrix is

different model. The design variables X1, X2, X3, and X4 make up the columns of the design matrix. This particular DOE has three levels of each design variable: -1, 0, and 1, where -1 would correspond to the original design variable value minus some percentage, 0 would correspond to the original design variable value, and 1 would correspond to the original design variable value plus some percentage. By looking at different combinations of the design variable levels, different models are created.

Design Variables →	No. #	X1	X2	X3	X4	f1(x)	f2(x)	f3(x)	← Responses
	1	-1.0	-1.0	-1.0	-1.0	1.2	50	9.8	
	2	-1.0	0.0	0.0	0.0	2.1	60	7.8	
	3	-1.0	1.0	1.0	1.0	2.0	66	7.7	
	4	0.0	-1.0	0.0	1.0	3.1	55	8.8	
	5	0.0	0.0	1.0	-1.0	1.9	53	9.1	
	6	0.0	1.0	-1.0	0.0	2.2	62	7.5	
	7	1.0	-1.0	1.0	0.0	2.7	51	8.1	
	8	1.0	0.0	-1.0	1.0	1.6	61	8.4	
	9	1.0	1.0	0.0	-1.0	2.4	59	9.5	

↑
Models

→ $f1(-1.0, 1.0, 1.0, 1.0) = 2.0$

Figure 4.4. Example design of experiments with responses.

Now that the DOE is completed, the models specified by the DOE are created. Finite element simulations are run on all the models, the responses of interest are recorded for each model. Fig. 4.4 shows the responses corresponding to each model. The responses of interest for structural design are stress, displacement, modal frequency, and strain. These responses are obtained from the finite element simulations. Other responses

of interest are weight, manufacturing cost, and complete cost. These responses are collected by other means and demonstrate the flexibility of the optimization technique. The responses recorded are defined by the user and could be anything that can be described by the design variables. The responses are added to the design matrix that is used in the next step of the process.

The next step is to create the metamodels. A metamodel is needed for each response. The metamodels are created using the DOE. For this study, a program called HIPPO developed at the Center for Advanced Vehicular systems was used (Fang and Horstemeyer, 2004). The DOE is given to HIPPO, and the user specifies the type of formulation to use. HIPPO will create both RSM and RBF surrogate models. HIPPO offers several basis functions to choose from when create RBF metamodels. There are other programs that will also perform this task. Similar routines have been developed in MATLAB and Excel (Solanki *et al.*, 2007), (Gu, Li, and Yang, 2004).

Once the metamodels have been obtained, the optimization problem must be defined. That is objects and constraints must be placed on the problem. Typically, the optimization problem would be given as:

$$\begin{array}{ll}
 \text{Minimize} & f_1(x_1, x_2, \dots, x_m) \\
 \\
 \text{s.t} & f_2(x_1, x_2, \dots, x_m) < \text{const.} \\
 & \vdots \\
 & f_n(x_1, x_2, \dots, x_m) < \text{const.} \\
 \\
 & x_i' \leq x_i \leq x_i'' \text{ for } i = 1, 2, \dots, m
 \end{array}$$

where n is the total number of responses, m is the number of design variables, x_i' is the lower bound of the i^{th} design variable, and x_i'' is the upper bound of the i^{th} design variable. In this formulation, the objective is to minimize $f_1(x_1, x_2, \dots, x_m)$ subject to a number of constraints on the other responses and limits on the design variables.

Now that the optimization problem is defined, it can be solved. HIPPO can be used to solve the optimization problem. HIPPO offers several optimization formulations such as global criteria, weighted sum, and non-linear formulation. The optimization problem is imported into HIPPO via text file that contains the metamodels and constraints. The user only needs to specify the formulation they desire to use, and HIPPO returns the optimal result. Once the metamodels have been created and the objectives and constraints are defined, the optimization problem becomes a math problem that can be solved using a number of methods in a number of programs. HIPPO was used because it conveniently integrates DOE, metamodeling, and an optimizing into one program. HIPPO is discussed in detail in Fang and Horstemeyer (2004). Other programs can be written to carry out design optimization. Programs have been written in MATLAB that will solve multi-objective design optimization problems. One such MATLAB program will be used in one of the case studies in the following chapters.

This section shows the ease of which multi-objective optimization can be performed. Using metamodeling techniques allows computational time to be reduced, and provides the user a lot of flexibility in defining the optimization problem. Once, the metamodels are produced the optimization problem can be defined and redefined with effort and little time. Fig 4.5 give an overview of the optimization process outlined above.

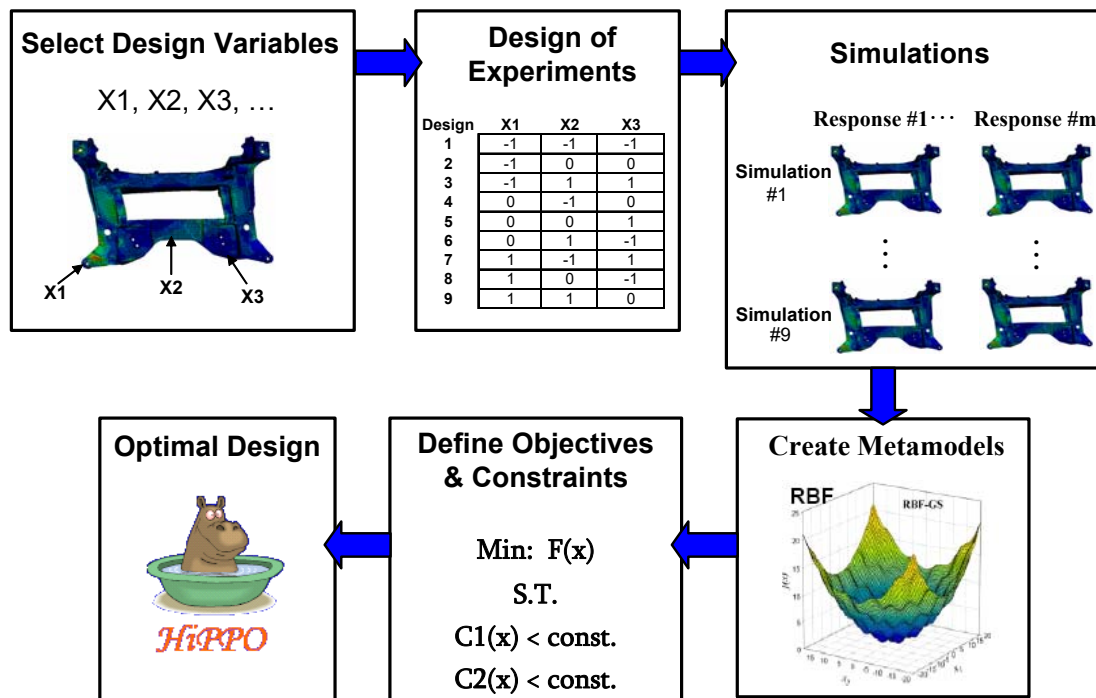


Figure 4.5. Design optimization overview.

CHAPTER V

CHEVROLET EQUINOX REAR SUBFRAME CASESTUDY

Introduction

The Chevrolet Equinox is an all wheel drive vehicle with front mounted engine, transmission, and transfer case. As part of a General Motors sponsored student project, Challenge X, a Chevrolet Equinox was outfitted with a turbo diesel engine and an electric motor to produce a hybrid version of the Equinox. The turbo diesel engine takes the place of the OEM gasoline burning engine and is used to power the front wheels of the vehicle. The stock drivetrain was removed, and a Ballard electric motor was placed between the rear wheels for power. The OEM rear drivetrain and electric rear drivetrain are shown in Fig 5.1. In order to accommodate the electric motor, the OEM rear cradle was redesigned. The goal for the Challenge X Equinox was to achieve superior fuel efficiency while maintaining or exceeding the performance of the stock vehicle. In order to meet this goal, the weight of the cradle must be reduced. As such, this research employed design optimization on the initial redesign of the cradle to help reduce the vehicle weight.

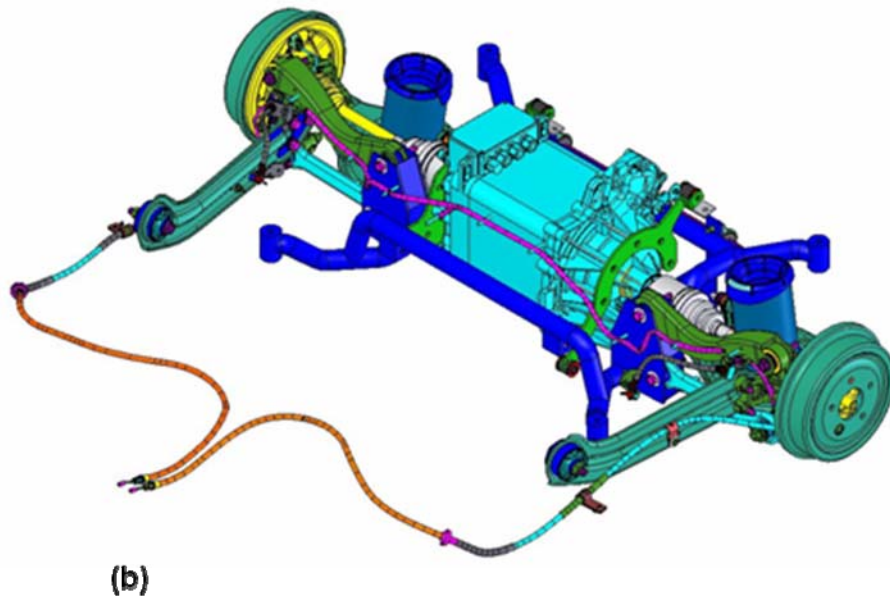
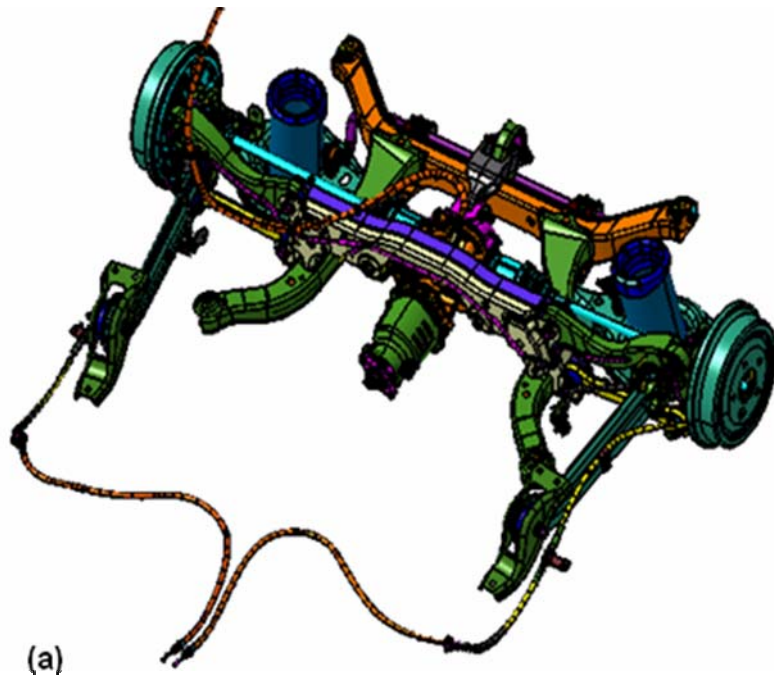


Figure 5.1. (a) Original Equinox drivetrain and rear subframe and (b) Challenge X designed electric drivetrain and rear subframe.

Subframe Construction

The new cradle needed to accommodate the electric motor and drive components for the hybrid setup. The new cradle comprised AISI 4130 round steel tubing and sheet. Four sections of mandrel bent tubes served to connect the suspension member mounting brackets to the Equinox chassis. The suspension member mounts were made from the steel sheet and were welded to the mandrel bent tubing. The OEM cradle design is shown in Figure 5.2 (a) along with the new cradle in Figure 5.2 (b). Bending the tubes reduced the number of welds required to make the cradle, and therefore reduced the number of stress concentrations induced by the welds. The bending process and round tubing also helped to make the cradle more easily manufactured compared to stock cradle consisting of multiple stampings welded together to form a box structure. The initial design of the cradle weighed 13.32 kg, which is approximately the same as the OEM cradle.

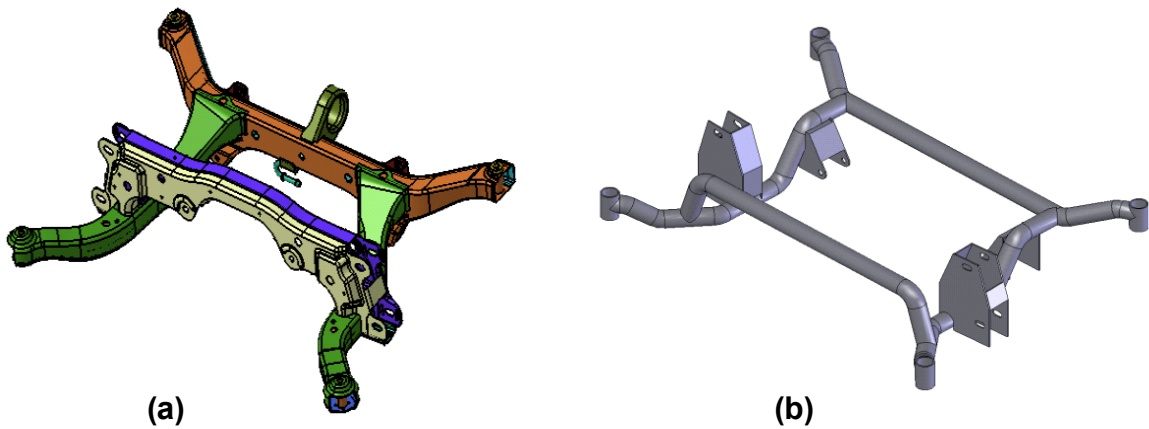


Figure 5.2. (a) OEM cradle design and (b) Challenge X cradle design.

Subframe Finite Element Simulation

A finite element model of the initial cradle design was created using quadratic tetrahedral elements. The C3D10 quadratic tetrahedral element is a 2nd order, 10 node element that addresses the issues of high shear and volumetric locking found in 1st order tetrahedral elements (ABAQUS 2002). The quadratic tetrahedral was chosen because of the ease in which the FE models can be generated. ABAQUS was used as the finite element program.

The FE model was constrained at the four mounts on the corners of the cradle. The suspension loads on the cradle were obtained from General Motors. Fifteen different load cases were obtained, and FE simulations were run using each load case. For the optimization, the load cases were limited for the sake of time. The results for the 15 simulations on the initial design were reviewed, and three load cases were selected for the optimization. The three selected load cases were the following: 0.5 G Reverse Panic Brake, 1.0G Cornering, and 2G/2G Bump. These three load cases were selected, because of their high amplitude forcing functions and their diversity of type. The 0.5 G Reverse Panic Brake loaded the vehicle in a more longitudinal manner; the 1.0G Cornering case loaded the vehicle in a transverse manner; and the 2G/2G Bump case loaded the vehicle in a vertical manner. The multiple, diverse cases were considered in the optimization to insure that the optimized design will meet requires for all of the load cases.

Subframe Optimization

The first step of the optimization process was to select the design variables. In the case of the cradle, twelve design variables were selected for optimization; they are shown in Fig 5.3. Once the number of design variables is known, the appropriate design of experiments can be selected. The Taguchi orthogonal array was selected to minimize the number of required simulations. The Taguchi orthogonal array does not consider all possible solutions like a full factorial, but it only requires 27 simulations in the case of twelve design variables where a full factorial would require 2197 simulations. The

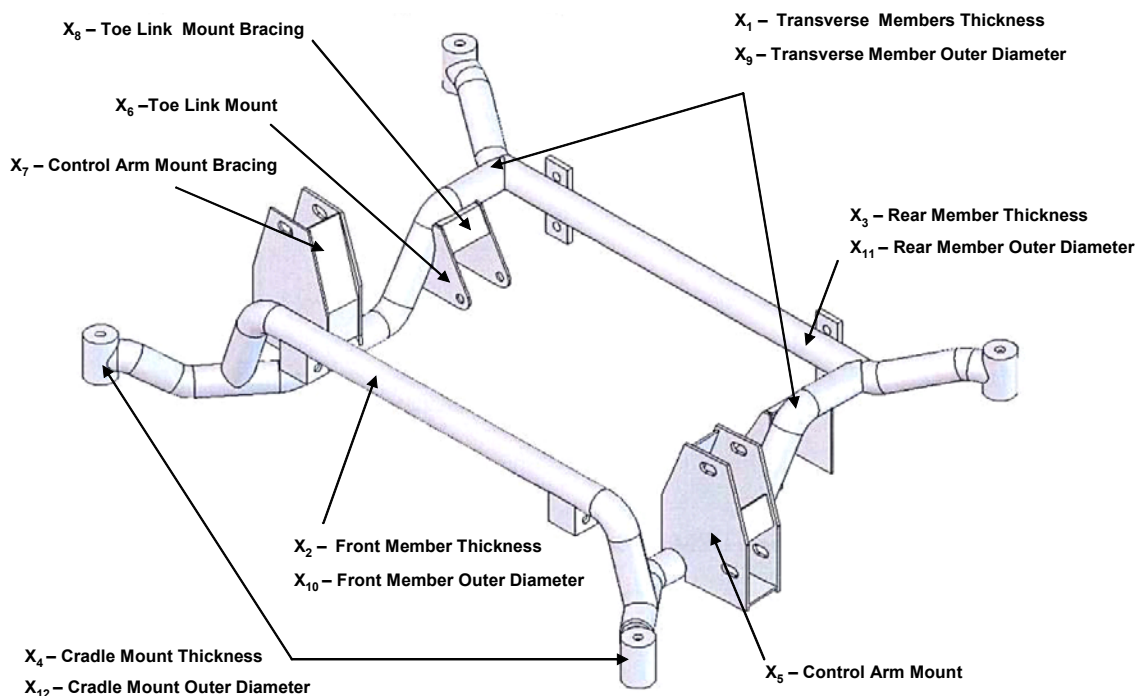


Figure 5.3. Chevrolet Equinox rear subframe optimization design variables.

Taguchi orthogonal array used was a three level L_{27} (Taguchi, 1993). The DOE is shown in Table 5.1. The three levels are -1, 0, and 1 and correspond to 25% less than the

original value, the original value, and 25% more than the original value. The number of rows of the design matrix is the number of required FE simulations. The simulation responses (von Mises stresses and displacements) correspond to the objects and constraints of the optimization problem. The responses are recorded in the design matrix (see Table 5.1), and the design matrix is used to create the metamodels. Radial Basis Functions (RBFs) were chosen for the metamodels, because of their high accuracy in highly complex

Table 5.1. Taguchi L_{27} design of experiments used of subframe optimization.

No.	X_1	X_2	X_3	X_4	X_5	X_6	X_7	X_8	X_9	X_{10}	X_{11}	X_{12}	$f_1(x)$	$f_2(x)$...	$f_{22}(x)$
1	-1	-1	-1	-1	-1	-1	-1	-1	-1	-1	-1	-1	68.657	1.00E+05	...	0.350
2	-1	-1	-1	-1	0	0	0	0	0	0	0	0	86.205	6.67E+04	...	0.150
3	-1	-1	-1	-1	1	1	1	1	1	1	1	1	113.734	4.20E+04	...	0.083
4	-1	0	0	0	-1	-1	-1	0	0	0	1	1	101.137	3.30E+04	...	0.104
5	-1	0	0	0	0	0	0	1	1	1	-1	-1	106.600	4.50E+04	...	0.145
6	-1	0	0	0	1	1	1	-1	-1	-1	0	0	99.964	5.80E+04	...	0.800
7	-1	1	1	1	-1	-1	-1	1	1	1	0	0	117.119	3.30E+04	...	0.083
8	-1	1	1	1	0	0	0	-1	-1	-1	1	1	109.322	5.00E+04	...	0.800
9	-1	1	1	1	1	1	1	0	0	0	-1	-1	112.541	3.30E+04	...	0.145
10	0	-1	0	1	-1	0	1	-1	0	1	-1	0	100.225	6.70E+04	...	0.145
11	0	-1	0	1	0	1	-1	0	1	-1	0	1	110.198	3.30E+04	...	0.104
12	0	-1	0	1	1	-1	0	1	-1	0	1	-1	108.577	5.00E+04	...	0.125
13	0	0	1	-1	-1	0	1	0	1	-1	1	-1	117.926	1.67E+04	...	0.083
14	0	0	1	-1	0	1	-1	1	-1	0	-1	0	99.364	5.00E+04	...	0.208
15	0	0	1	-1	1	-1	0	-1	0	1	0	1	121.452	3.30E+04	...	0.104
16	0	1	-1	0	-1	0	1	1	-1	0	0	1	99.660	3.30E+04	...	0.125
17	0	1	-1	0	0	1	-1	-1	0	1	1	-1	117.944	3.00E+04	...	0.104
18	0	1	-1	0	1	-1	0	0	1	-1	-1	0	108.966	2.50E+04	...	0.125
19	1	-1	1	0	-1	1	0	-1	1	0	-1	1	114.622	5.00E+04	...	0.125
20	1	-1	1	0	0	-1	1	0	-1	1	0	-1	110.941	5.00E+04	...	0.145
21	1	-1	1	0	1	0	-1	1	0	-1	1	0	124.146	2.50E+04	...	0.083
22	1	0	-1	1	-1	1	0	0	-1	1	1	0	107.168	4.00E+04	...	0.145
23	1	0	-1	1	0	-1	1	1	0	-1	-1	1	104.766	6.67E+04	...	0.200
24	1	0	-1	1	1	0	-1	-1	1	0	0	-1	123.342	3.30E+04	...	0.104
25	1	1	0	-1	-1	1	0	1	0	-1	0	-1	108.863	3.30E+04	...	0.104
26	1	1	0	-1	0	-1	1	-1	1	0	1	0	133.083	2.50E+04	...	0.083
27	1	1	0	-1	1	0	-1	0	-1	1	-1	1	115.400	3.30E+04	...	0.145

engineering problems. The optimization problem is written in terms of the objective and the constraints as:

$$\begin{aligned}
& \text{Minimize} && f_1(x_1, x_2, \dots, x_{12}) \\
& \text{s.t} && f_2(x_1, x_2, \dots, x_{12}) < \text{const.} \\
& && \vdots \\
& && f_{22}(x_1, x_2, \dots, x_{12}) < \text{const.} \\
& && x_i' \leq x_i \leq x_i'' \text{ for } i = 1, 2, \dots, 12
\end{aligned}$$

Setting up the optimization problem in this fashion allows a multi-objective problem to be simplified to a single objective. The objective minimizes mass while keeping the stress and stiffness of the cradle below a certain level. In the case of the cradle, the stress was monitored in all four tubular components and in the control arm mounts and toe link mounts, and the displacement was monitored in the control arm mounts and toe link mounts. A total of twenty-one constraints were specified for the cradle optimization problem (seven constraints per load case for three load cases). The stress constraints were set to 448 MPa, and the displacement constraints were set to 3.81 mm. The optimization is also bound geometrically. Each design variable has an upper boundary, x_i'' , and lower boundary, x_i' . The upper and lower bounds correspond to the $\pm 25\%$ used for the design of experiments.

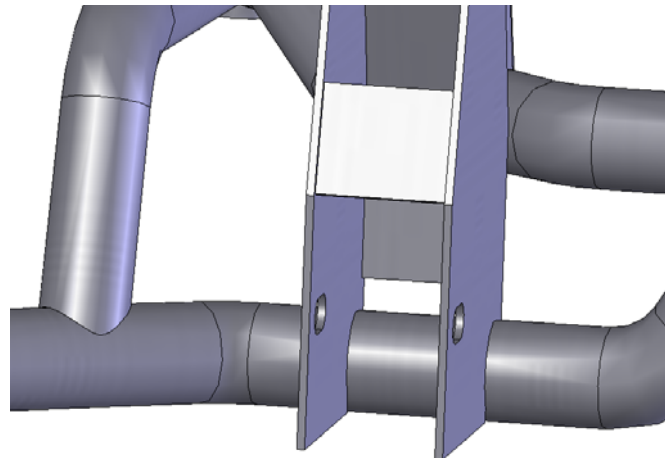
Once the objectives and constraints were specified, HiPPO analyzed the metamodels representing the objectives and constraints functions and found an optimal design. A FE simulation of the optimized design similar to that of the initial cradle design was run, and the results were compared to that of the initial design.

Optimization Results

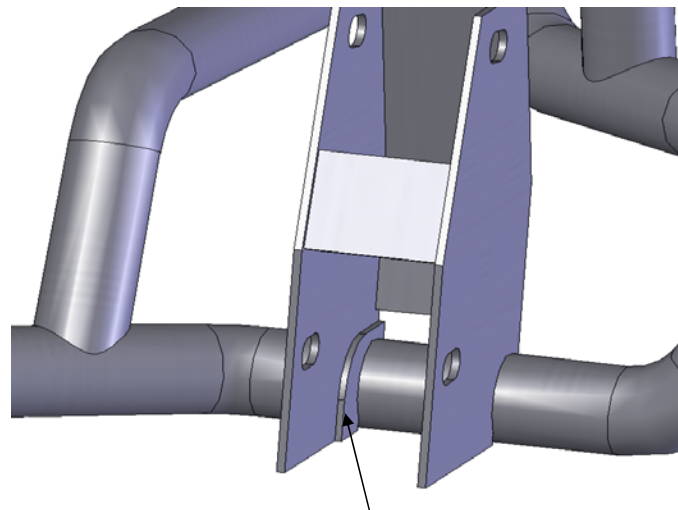
The design variable values for the optimized design along with the initial design variable values are shown in Table 5.2. The optimized design has a weight of 11.37 kg where the initial design has a weight of 13.32 kg, a reduction of 12%. The FE simulation of the optimized design showed high stress where the control arm mount connects to the transverse cradle tube. Additional material was added to this area to reduce the high stresses. Even with this added mass in this region the overall weight savings was still 12%. This new design is illustrated in Fig 5.4. The additional material brought the stress level down to between 350 and 400 MPa, which is below the yield strength of the material. Results of the FE simulations of the new design are shown in Fig 5.5 illustrating the areas of highest stress for the optimized design; Fig 5.6 shows the corresponding areas for the initial design. The stress in the optimized cradle is slightly lower where the control arm mount connects to it, and the stress in the control arm mount is much lower in the optimized case than the original case (see Fig 5.5 (c) and Fig 5.6 (c)). Other areas of the cradle that had very low stresses in the initial design had higher stresses in the optimized design. This can be observed in Fig 5.5 (b) and 5.6 (b). The higher stress is due to the removal of excess material in the optimization process. The stress in the area is only about 350 MPa, which is well below yield. The displacement in the optimized cradle is 5.08 mm and is found in the toe link mount (see Fig 5.5 (a)). Although this 1.4 mm displacement is greater than the displacement in the initial cradle design of 3.7 mm (see Fig 5.6 (a)), the increased displacement is still admissible.

Table 5.2. Initial and optimized design variable values in millimeters

	X_1	X_2	X_3	X_4	X_5	X_6	X_7	X_8	X_9	X_{10}	X_{11}	X_{12}
Int.	3.05	3.05	3.05	3.05	3.81	3.81	3.81	3.81	41.28	41.28	41.28	41.28
Opt.	3.28	2.29	2.29	2.29	2.86	2.86	2.86	4.76	40.72	36.25	30.99	30.99



(a) Cradle before additional material was added



(b) Cradle with additional material added at stress concentration

Figure 5.4. Additional material added to reduce stress concentration where control bracket meets transfers tube.

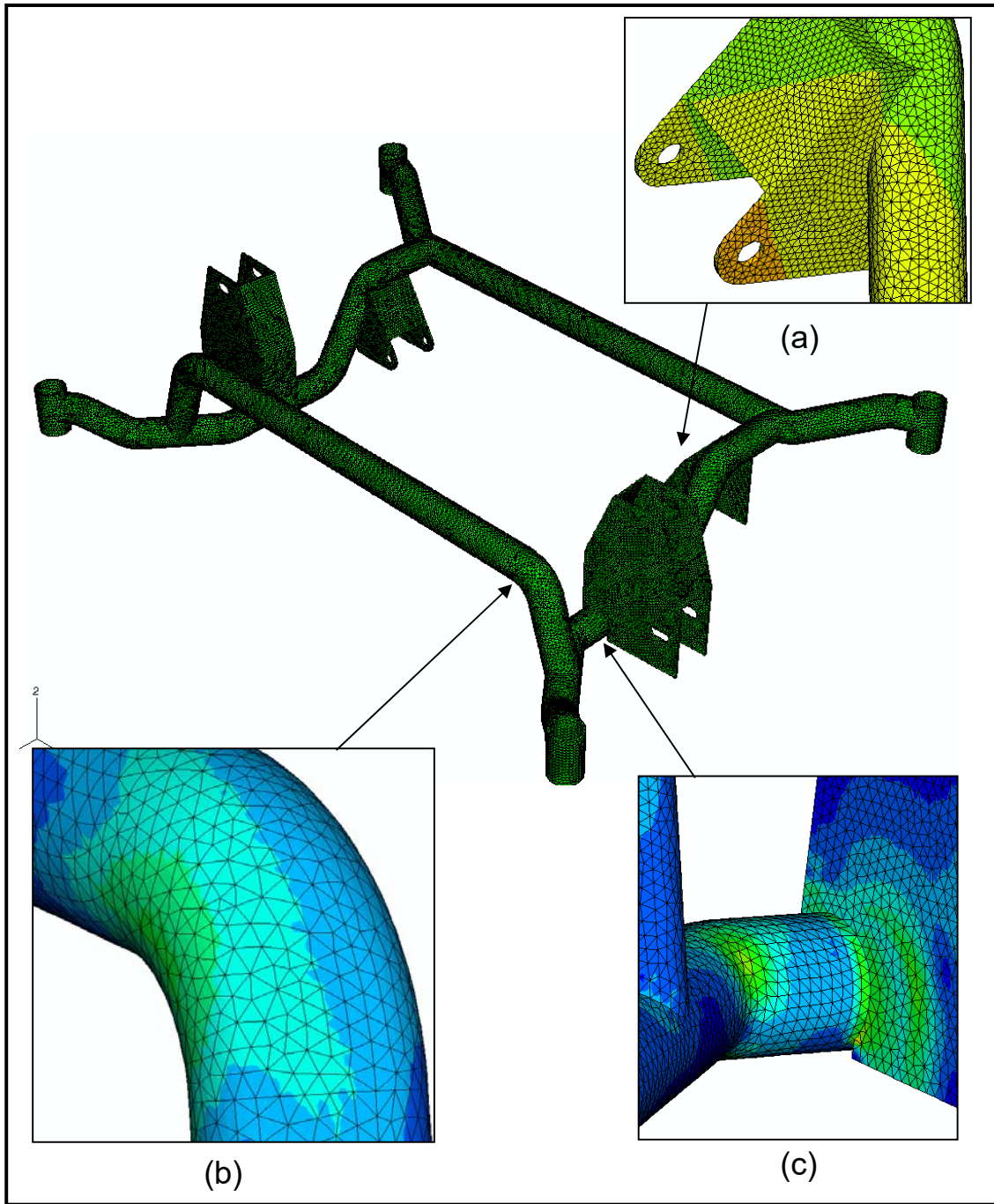


Figure 5.5. Optimized cradle (a) displacement from 0.5G Rev Panic brake load case and (b) and (c) stress from 2G/2G Bump load case.

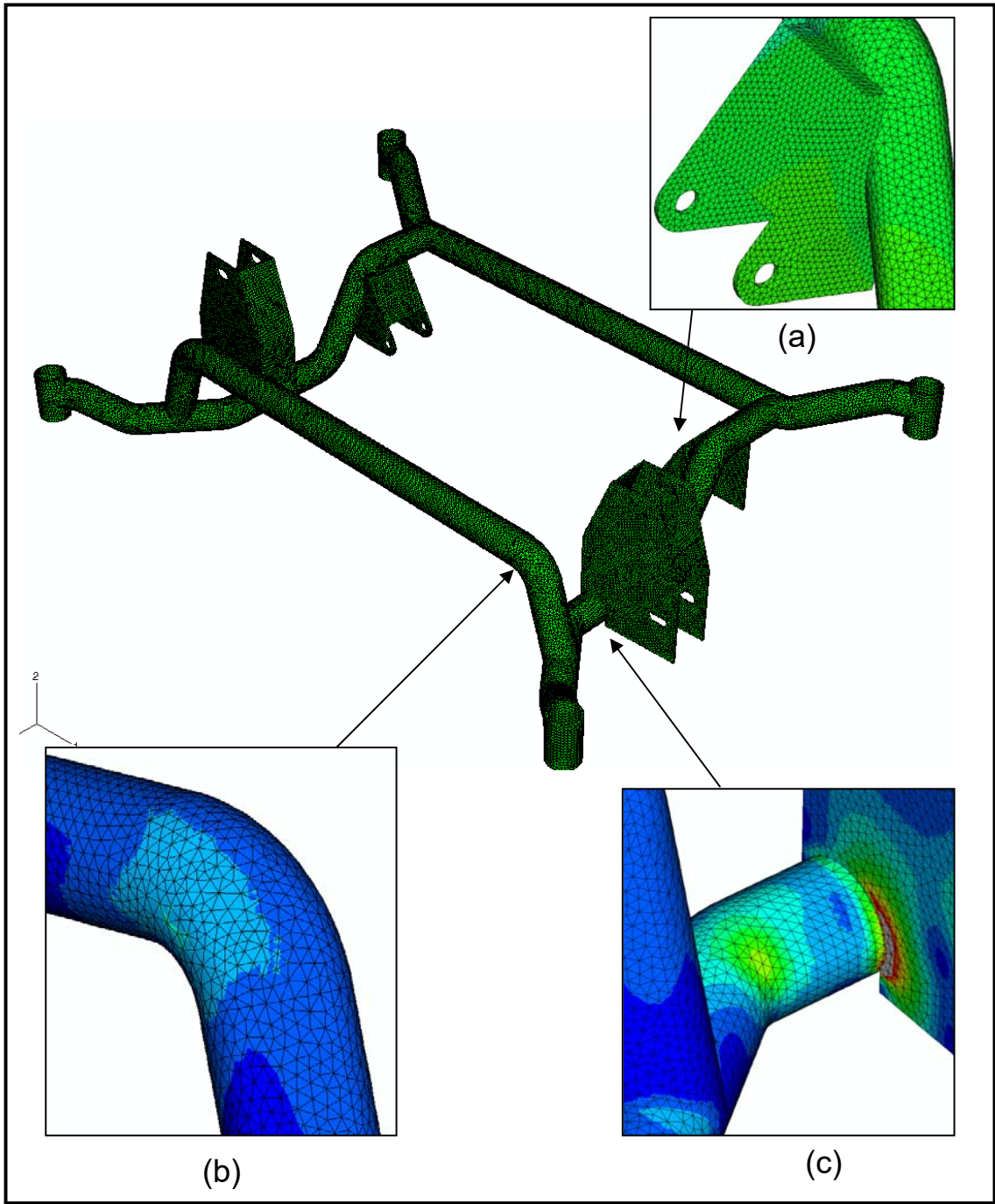


Figure 5.6. Initial cradle (a) displacement from 0.5G Rev Panic brake load case and (b) and (c) stress from 2G/2G Bump load case.

Conclusion

A redesigned Chevrolet Equinox rear cradle was optimized to reduce weight. To perform the optimization, the multi-objective design optimization routine outlined in the previous chapter was employed. Twelve design variables and 22 responses were selected for the optimization problem. Twenty-two RBF representing the cradle's weight, stresses, and displacements were created using relatively small finite element simulation samples. The optimization problem was written such that the multi-objective problem was reduced to a single objective with multiple constraints, the objective being the weight of the cradle and the constraints being the stress and displacement levels. The optimization software HIPPO was used to minimize the object subject to the given constraints. The optimal design was found to reduce the weight by 12%. The optimal solution was validated using a FE simulation. Some small changes were made to relieve stress concentrations, but the 12% weight reduction was still maintained.

CHAPTER VI

FORMULA SAE UPRIGHT CASESTUDY

Introduction

The Formula SAE competition is a yearly design competition held in Detroit, Michigan and is hosted by the Society of Automotive Engineers (SAE). The competing teams are to design and build a Formula One style car to compete in a number of static and dynamic events. The weight of the vehicle is imperative to vehicle performance in all the dynamic events and also plays a large role in the design and cost events. In order to be more competitive in the 2007 competition, the Mississippi State University Formula SAE Team set a goal to reduce the vehicle weight by 25%. In order to meet this goal, the front upright must be redesigned, and weight of the upright must be reduced. The upright connects the upper and lower control arms to the wheel and hub assembly. Fig 6.1 shows the upright assembled to the control arms and hub. The isolated upright is shown in Fig. 6.2. As such, this research employed design optimization on the redesign of the upright to help reduce the vehicle weight in order to achieve the team's weight reduction goal.

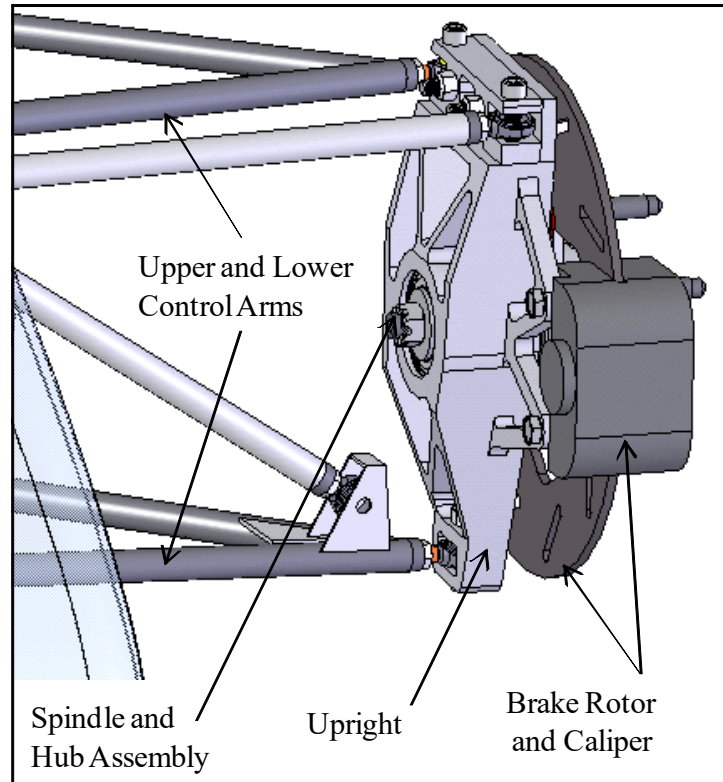


Figure 6.1. Formula SAE front upright assembly with control arms and brake rotor and caliper.

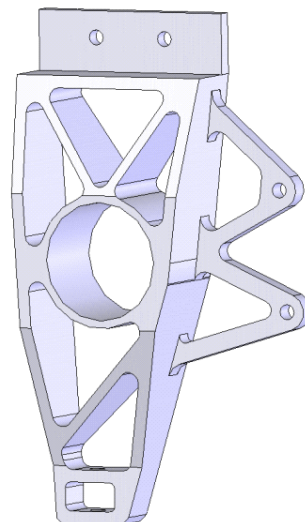


Figure 6.2. Formula SAE front upright shown with no parts assembled.

Initial Upright Design

The initial upright design was based off of the 2006 design with a few key changes. The first change was to integrate the brake caliper mounting bracket and the upright into a single part. The second change was to add a series of webs to the upright to improve the rigidity of the upright. Rigid is very important in suspension component design. All the motion of the suspension should take place through the translation of the components and not the deflection or flexing of the components while under load. Fig 6.3 shows the 2006 design and initial 2007 upright designs. The upright is constructed of 6061-T6 wrought aluminum. This material was selected for its light weight, inexpensive cost, availability, and machinability. The weight of the 2006 design is 0.953 kg, and the weight of the initial 2007 design is 0.826 kg. This is a 13% weight reduction. This was achieved by adding the webs to maintain rigidity while decreasing all the wall thicknesses to reduce weight. Even with a 13% weight reduction, there are still areas where stress is very low. So, more mass can be removed using an optimization routine.

A finite element model of the initial upright design was created using quadratic tetrahedral elements. The C3D10 quadratic tetrahedral elements used for the Equinox rear subframe models were used again, and again ABAQUS was used as the finite element program. The FE models range from 250,000 elements to 350,000 elements. The finite element simulations used an ISV plasticity model for the 6061-T6 AL. The upright was constrained by the mounting points for the upper and lower control arms. Three load cases were considered 1.5G cornering, 1.25G braking, and 1.0gG curb impact. The load calculations are given in Appendix A. The cornering and braking loads are the most sever

loads seen by this type of car. The 1.0G curb impact was added as a precaution to insure that the car could sustain some type of impact without experiencing failure. The loads were calculated using hand calculation methods and were based off the characteristics of the 2006 car design. A factor of safety of 2.0 was added to the loads to account for the uncertainties in the calculations and vehicle design assumptions. The use of a vehicle dynamics program and a more complete 2007 vehicle design would help to reduce the factor of safety.

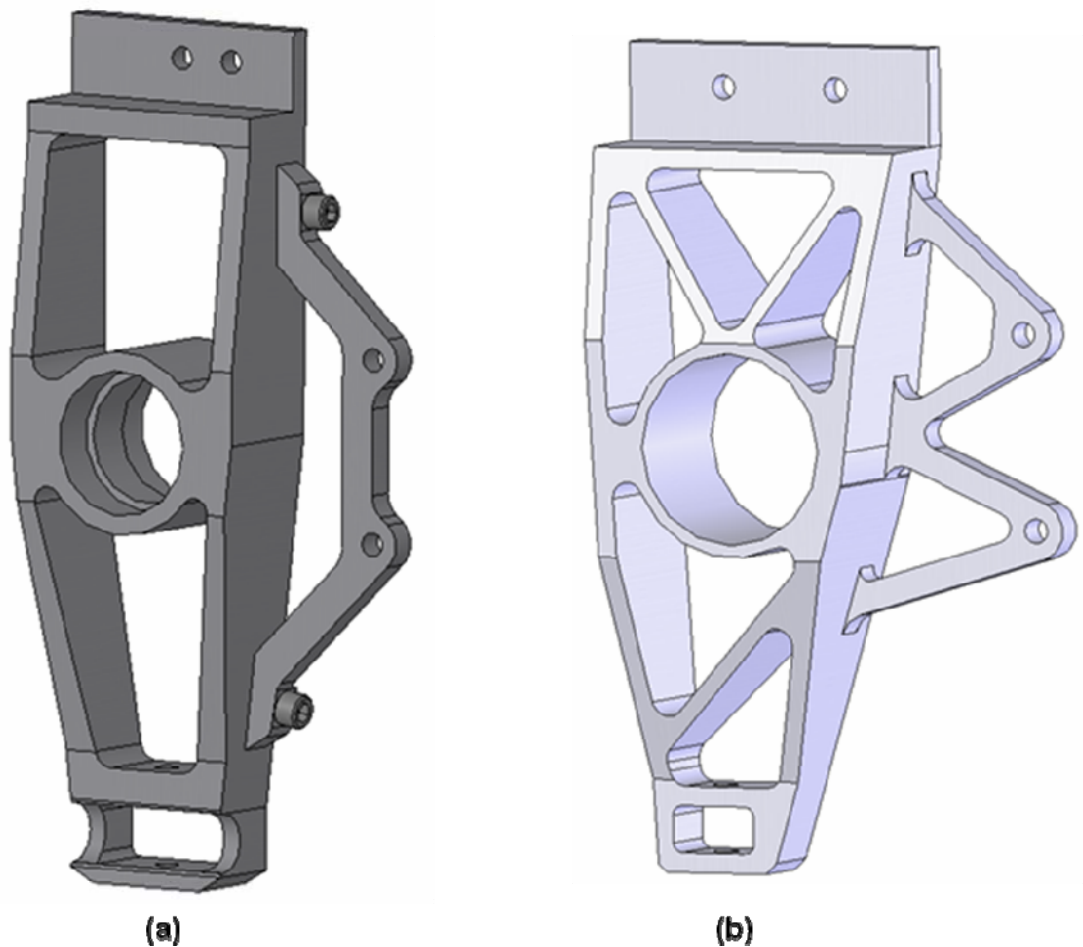


Figure 6.3. The 2006 Formula SAE front upright design (a) and the 2007 front upright design (b).

Upright Optimization

The first step in the upright optimization was to select the design variables. The design variables were selected so that any changes made during the optimization process would not change the functionality of the upright. Twelve design variables were selected for optimization. The web structure that serves to tie all the main features of the upright together and the caliper mounting bracket were selected. The design variables are shown in Fig 6.4. Finite element simulations ran on the initial design revealed that the damage level, stress level, and displacement were very low. With this being the case, it was decided to lower the optimization starting point to insure that all excess mass could be removed. The initial design variable values and optimization starting point values are shown in Table 6.1.

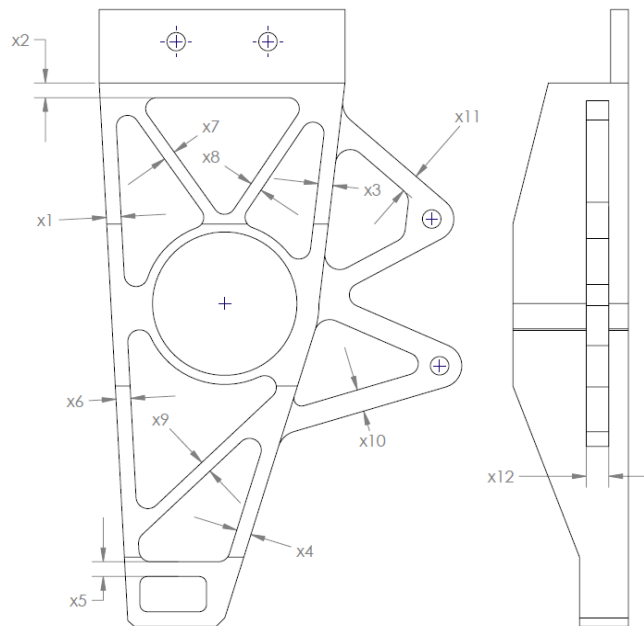


Figure 6.4. Front upright optimization design variables.

Table 6.1. Initial upright design variable values and starting point values in millimeters.

Variable	x1	x2	x3	x4	x5	x6	x7	x8	x9	x10	x11	x12
Initial	6.35	6.35	6.35	6.35	6.35	6.35	5.08	5.08	5.08	9.53	8.13	9.65
Starting	4.76	4.76	4.76	4.76	4.76	4.76	3.81	3.81	3.81	8.27	6.10	7.24

The next step was to select a DOE. The Taguchi L_{27} was selected on its ability to reduce the number of required simulations. As mentioned earlier, the L_{27} is a three level DOE meaning that each design variable has three levels. In the case of the upright, the three levels are +25%, starting, and -25%. A higher density of design points is achieved by keeping the bounds of the design variables relatively small. This is why it was important to choose starting point values lower than the initial design values instead of increasing the bounds of the design variables. By increasing the bounds, the same amount of design points would be spread over a larger area, and this could lead to larger errors in the metamodels. The DOE for the upright design is given in Table 6.2. The columns of Table 6.2 are the design variable values, and the rows of Table 6.2 are the required models.

FEA were run on each of the models specified in the DOE. The FEA used the ISV plasticity damage model discussed earlier in this paper. The responses of interest were collected from the simulations. These responses were recorded and used to create the metamodels for the optimization.

Table 6.2. Taguachi L_{27} DOE used for front upright optimization (all values are in millimeters).

	x1	x2	x3	x4	x5	x6	x7	x8	x9	x10	x11	x12
1	3.57	3.57	3.57	3.57	3.57	3.57	2.86	2.86	2.86	6.20	4.57	5.43
2	3.57	3.57	3.57	3.57	4.76	4.76	3.81	3.81	3.81	8.27	6.10	7.24
3	3.57	3.57	3.57	3.57	5.95	5.95	4.76	4.76	4.76	10.33	7.62	9.05
4	3.57	4.76	4.76	4.76	3.57	3.57	2.86	3.81	3.81	8.27	7.62	9.05
5	3.57	4.76	4.76	4.76	4.76	4.76	3.81	4.76	4.76	10.33	4.57	5.43
6	3.57	4.76	4.76	4.76	5.95	5.95	4.76	2.86	2.86	6.20	6.10	7.24
7	3.57	5.95	5.95	5.95	3.57	3.57	2.86	4.76	4.76	10.33	6.10	7.24
8	3.57	5.95	5.95	5.95	4.76	4.76	3.81	2.86	2.86	6.20	7.62	9.05
9	3.57	5.95	5.95	5.95	5.95	5.95	4.76	3.81	3.81	8.27	4.57	5.43
10	4.76	3.57	4.76	5.95	3.57	4.76	4.76	2.86	3.81	10.33	4.57	7.24
11	4.76	3.57	4.76	5.95	4.76	5.95	2.86	3.81	4.76	6.20	6.10	9.05
12	4.76	3.57	4.76	5.95	5.95	3.57	3.81	4.76	2.86	8.27	7.62	5.43
13	4.76	4.76	5.95	3.57	3.57	4.76	4.76	3.81	4.76	6.20	7.62	5.43
14	4.76	4.76	5.95	3.57	4.76	5.95	2.86	4.76	2.86	8.27	4.57	7.24
15	4.76	4.76	5.95	3.57	5.95	3.57	3.81	2.86	3.81	10.33	6.10	9.05
16	4.76	5.95	3.57	4.76	3.57	4.76	4.76	4.76	2.86	8.27	6.10	9.05
17	4.76	5.95	3.57	4.76	4.76	5.95	2.86	2.86	3.81	10.33	7.62	5.43
18	4.76	5.95	3.57	4.76	5.95	3.57	3.81	3.81	4.76	6.20	4.57	7.24
19	5.95	3.57	5.95	4.76	3.57	5.95	3.81	2.86	4.76	8.27	4.57	9.05
20	5.95	3.57	5.95	4.76	4.76	3.57	4.76	3.81	2.86	10.33	6.10	5.43
21	5.95	3.57	5.95	4.76	5.95	4.76	2.86	4.76	3.81	6.20	7.62	7.24
22	5.95	4.76	3.57	5.95	3.57	5.95	3.81	3.81	2.86	10.33	7.62	7.24
23	5.95	4.76	3.57	5.95	4.76	3.57	4.76	4.76	3.81	6.20	4.57	9.05
24	5.95	4.76	3.57	5.95	5.95	4.76	2.86	2.86	4.76	8.27	6.10	5.43
25	5.95	5.95	4.76	3.57	3.57	5.95	3.81	4.76	3.81	6.20	6.10	5.43
26	5.95	5.95	4.76	3.57	4.76	3.57	4.76	2.86	4.76	8.27	7.62	7.24
27	5.95	5.95	4.76	3.57	5.95	4.76	2.86	3.81	2.86	10.33	4.57	9.05

Using the DOE and collected responses, the desired metamodells were created.

The metamodells correspond to the responses of interest, and in this case the responses of interest were mass, damage level, displacement, and natural frequency. Eight metamodells corresponding to the mass, damage for each of the three load cases, displacement for each of the three load cases, and natural frequency were formulated. The metamodells were created using a MATLAB program written by Solanki *et al.*, (2007). The surrogate models were RBF using an inverse-multiquadratic basis function.

Next the optimization problem was defined. The objective of the problem is to minimize mass. The constraints on the problem are the damage level, displacement level, and natural frequency. The maximum allowable damage level is 0.1. This insures that the elastic modulus does not become degraded which would lead to failure. The displacement level was set at 0.75 mm. The displacement constraint insured that the wheel bearings housed in the upright would not see excessive misalignment that would lead to decreased bearing life and eventually failure of the bearings. It was desired to keep the natural frequency of the part as high as possible to insure that the stiffness of the part was maintained. Rigidity of suspension members is very important to ensure that the suspension will perform as intended. So, the natural frequency level was not to drop below 2000 Hz. The upright optimization problem can be written as

$$\begin{aligned}
 & \text{Minimize} && f_1(x_1, x_2, \dots, x_{12}) \\
 & \text{s.t} && c_1(x_1, x_2, \dots, x_{12}) < \text{const.} \\
 & && \vdots \\
 & && c_6(x_1, x_2, \dots, x_{12}) < \text{const.} \\
 & && c_7(x_1, x_2, \dots, x_{12}) > \text{const.} \\
 & && x_i' \leq x_i \leq x_i'' \text{ for } i = 1, 2, \dots, 12
 \end{aligned}$$

where, x_i'' , and x_i' are the upper and lower bounds corresponding to the $\pm 25\%$ used for the design of experiments. This constraints the design space within the sampling space. The optimization problem was solved using a MATLAB program that utilizes the MATLAB optimization tool box (MathWorks, 2007). The program was written by Solanki *et al.*, (2007).

Optimization Results

The design variable values for the optimized design along with the initial design variable values are given in Table 6.3. All the design variables were reduced significantly except design variable 10 that increased to increase strength in the area. FEA was used to find the responses of the optimized design. Table 6.4 gives the responses of the optimized design and the initial design. The mass of the upright was reduced from 0.826 kg to 0.643 kg, a 22% reduction.

Table 6.3. Optimized and initial design variable values given in millimeters.

	x1	x2	x3	x4	x5	x6	x7	x8	x9	x10	x11	x12
org	6.35	6.35	6.35	6.35	6.35	6.35	5.08	5.08	5.08	9.52	8.12	9.65
opt	3.57	3.57	3.57	3.57	5.95	3.57	2.86	4.76	2.86	10.33	7.62	5.43

Table 6.4. Finite element responses for both the optimized and initial upright designs.

	mass	NF	
initial	0.826	3187	
optimized	0.643	2788	
1.25G Braking			
	stress	damage	disp
initial	227.3	1.0000E-04	0.348
optimized	294.4	1.0150E-04	0.650
1.5G Cornering			
	stress	damage	disp
initial	171.1	1.0010E-04	0.501
optimized	269.0	1.0540E-04	0.790
1.0G Curb Impact			
	stress	damage	disp
initial	115.7	1.0000E-04	0.146
optimized	207.7	1.0000E-04	0.209

The damage level, stress level and displacement increased in the optimized design. Fig 6.5 shows the stress contour plot for 1.5G cornering load case for the optimized design. The stress level has increased but has become more distributed over the upright. Fig 6.5 can be compared to Fig 6.6 of the initial design to see that areas that had almost no stress (upper webs and lower left web) are now seeing higher stress. The optimization has removed excess material from the low stress areas in order to reduce weight.

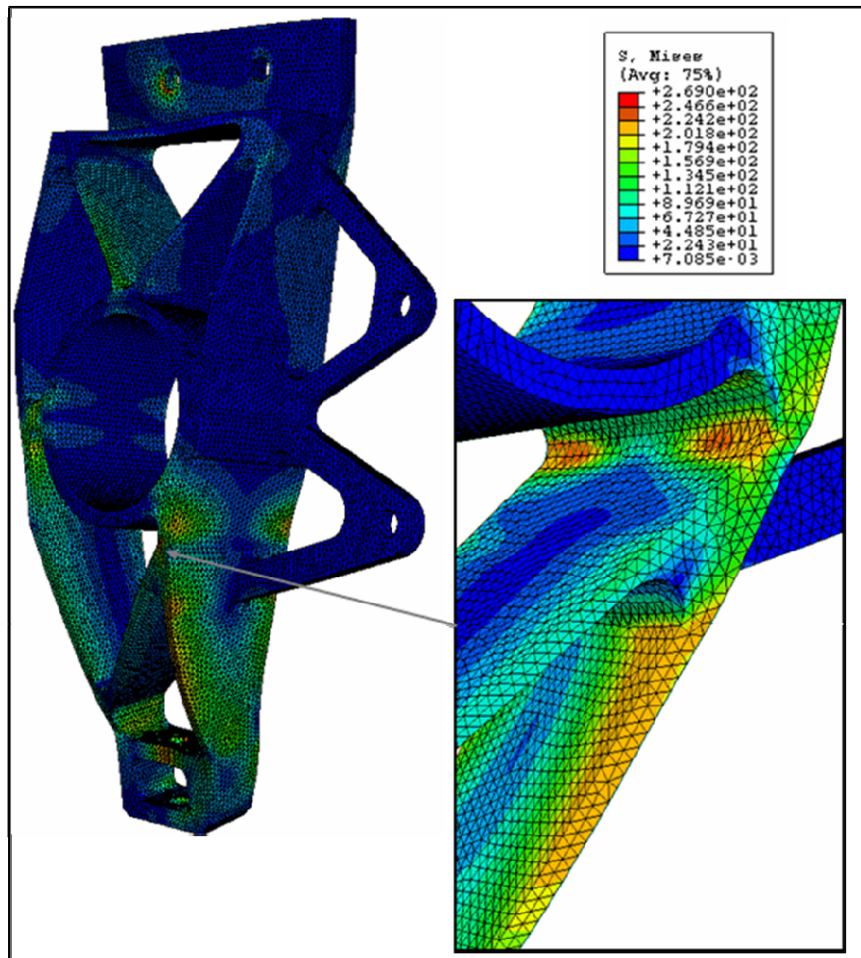


Figure 6.5 Stress contour plot for 1.5G cornering load for optimized design in MPa.

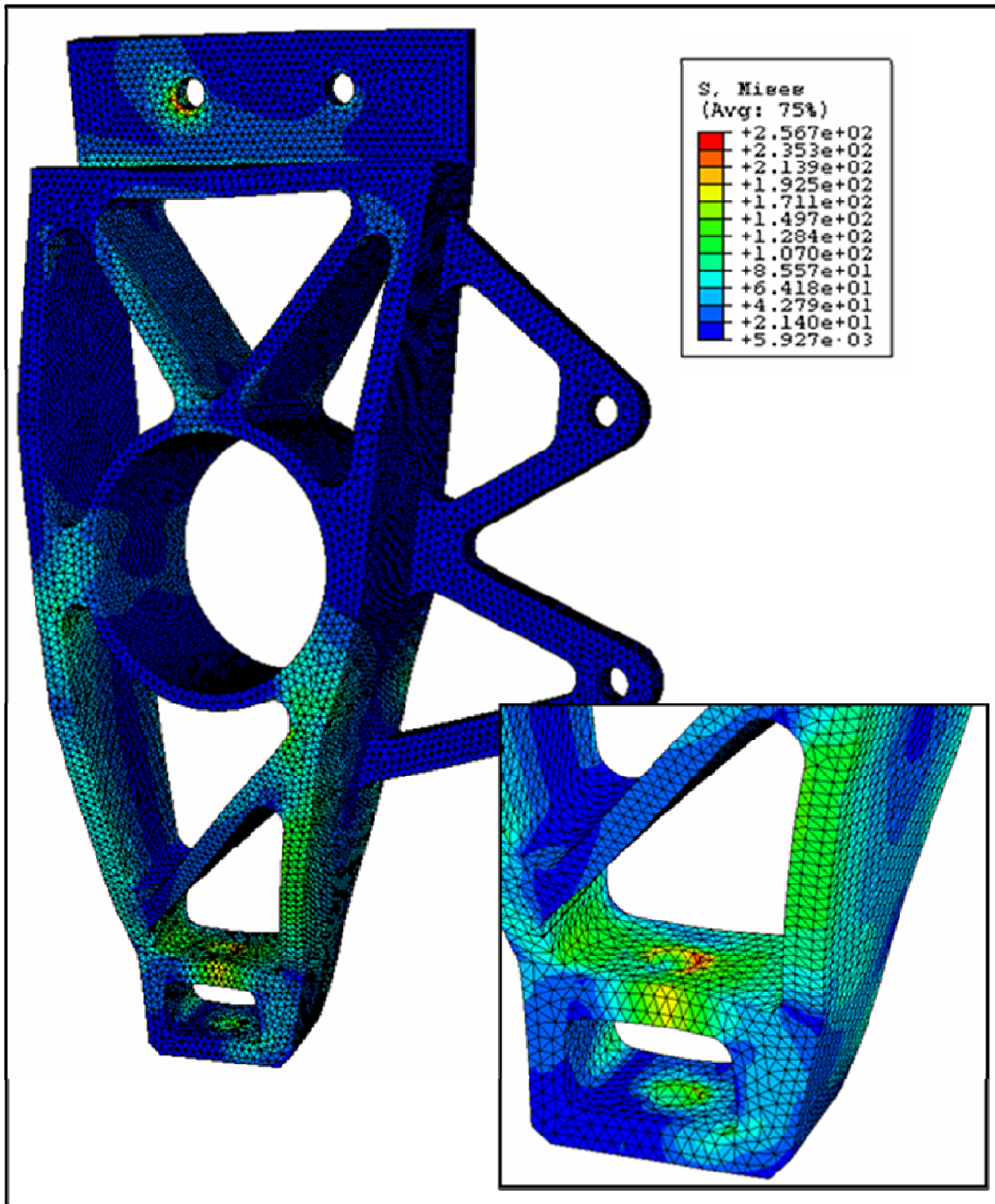


Figure 6.6 Stress contour plot for 1.5G cornering load for initial design in MPa.

In the 1.25G braking load case, the stress level in the optimized design is actually above the yield strength of the material (275 MPa), but the damage level is below the failure criteria of 0.1. So, the design is still safe. Table 6.4 shows that the stress is higher in the 1.25G braking than in the 1.5G cornering case, but damage is actually higher in the 1.5G cornering than in the 1.25G braking case. Damage contour plots for the 1.25G braking load case for the optimized and initial designs are shown in Fig 6.7 and Fig 6.8 respectively. Fig 6.7 shows that the damage is very low and isolated to only a few spots on the upright. Fig 6.8 shows that the damage level is at the initial material damage level.

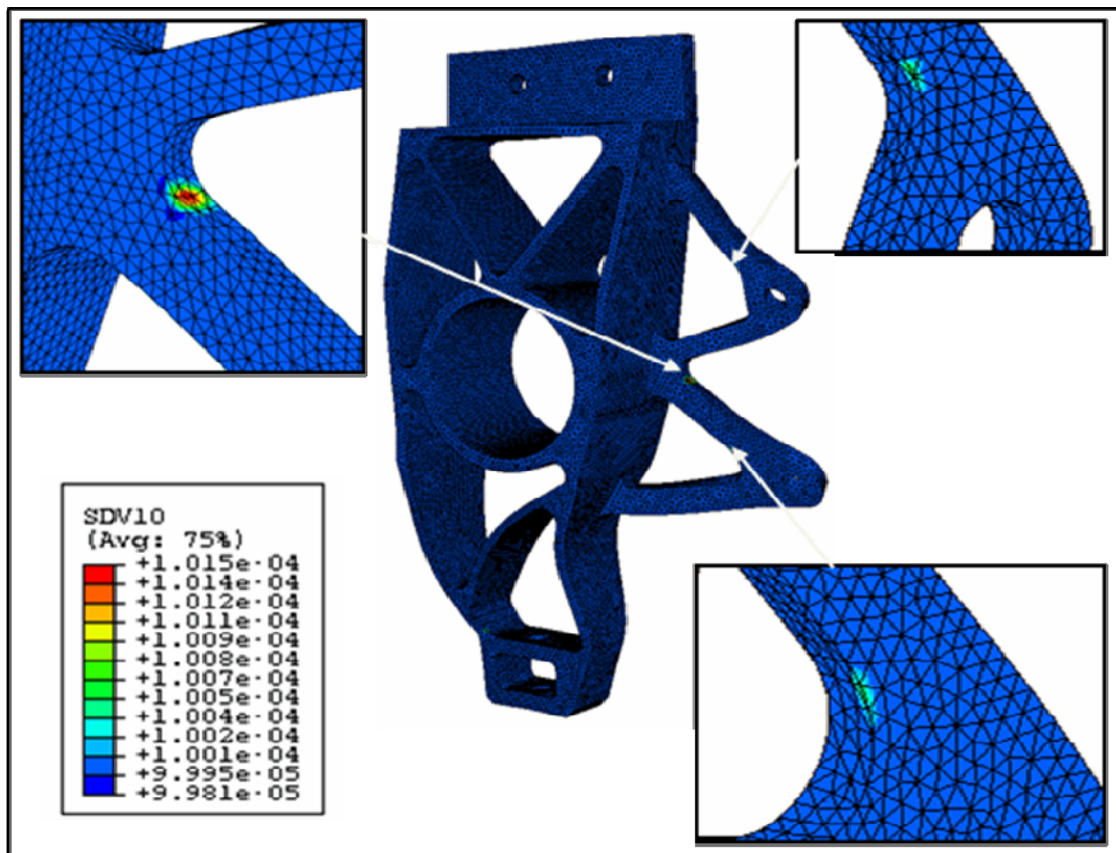


Figure 6.7. Damage (SDV10) contour plots for 1.25G braking load case for optimized design.

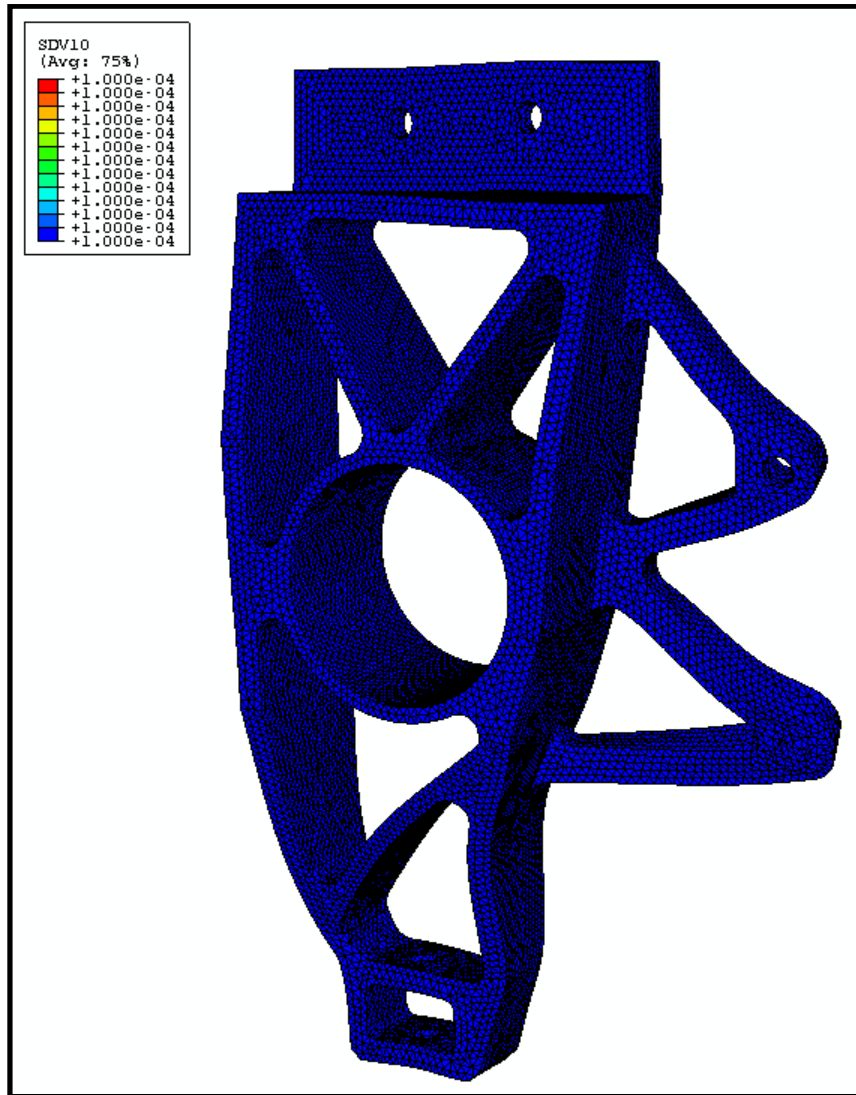


Figure 6.8. Damage (SDV10) contour plots for 1.25G braking load case for initial design.

The displacement was increased in all load cases in the optimized above the initial level. In the 1.5 braking case, the displacement is slightly above the constraint set on displacement in the optimization. This is due to error in the approximation models. The

displacement is small enough that design is still acceptable. The natural frequency did drop, but it is much higher than the constraint placed on it.

Conclusion

The front upright from the 2007 Formula SAE car was optimized to reduce weight in order to meet a design goal of 25% total vehicle weight reduction. To achieve this goal a multi-objective design optimization routine was employed that used metamodels and an ISV plasticity damage material model. Twelve design variables were selected for optimization. Eight responses were approximated using metamodeling techniques and finite element simulations. The objective of the problem was to minimize mass with constraints on damage level, displacement, and natural frequency. A MATLAB program was used to find the optimal design while still meeting all the constraints. The optimized design provided a 22% weight reduction in the part from the initial design. The damage level was below the failure criteria in all cases even though the von Mises stress was higher than yield in one case. It was also seen that the damage was actually lower in the case with the highest stress than in another case where the stress was much lower. The displacement levels were within acceptable limits of the constraints, and the natural frequency was well within the limited placed on it.

CHAPTER VII

CONCLUSION AND SUMMARY

In this document, a design tool has been outlined that will help to meet stringent design criteria while reducing development time. This tool is multi-objective design optimization using metamodeling techniques and ISV plasticity damage material models. Multi-objective design optimization will consider multiple load cases in order to meet the objective of the design problem while staying within all constraints. In order to reduce computing time, surrogate models are used to approximate responses of the part or system being optimized. Metamodels require very little computing power. So, the problem objectives and constraints can be changed, and the optimized design can be recalculated in a very short time. The ISV plasticity damage material model provides for the history of the material microstructure to be considered throughout the design process. Material characteristics on the nano, micro, and meso scales are incorporated into the ISV plasticity damage model so that their effects can be seen on the macroscale.

Two studies were conducted using multi-objective design optimization. The first was on a vehicle rear subframe. The subframe study considered three load cases and over twenty constraints. The optimized design had higher stress in areas with very low stress initially and lower stress in areas that initially had very high stress. The end result was a

subframe that was 12% lighter and that actually met design requirements that the initial design did not.

The second study was carried out on a Formula SAE front upright. The front upright optimization involved three load cases and seven constraints. An ISV plasticity damage material model for 6061-T6 AL was implemented into the FEA of the upright, and the damage level was used for the failure criteria. The optimized upright showed an increase in stress in areas of low stress initially. The damage level also increased but was well under the failure level. It was seen that damage provided a better failure criteria than the von Mises stress. Areas with high von Mises stress had little or no damage. The displacement proved to be the limiting response on the optimization. The displacement in one load case of the optimized design was slightly over the constraint placed on it due to metamodeling error, but the amount was so small that the optimized design was still acceptable. A 22% weight saving was achieved on the upright design by employing multi-objective design optimization.

The case studies showed the gains that can be made by using multi-objective design optimization in the design process. This process can be used to meet increasingly tougher design requirements without increasing product development time. The metamodeling techniques reduce computation time, and the ISV plasticity damage material model provides a safe design. Together, these techniques can equip the designers with a tool to meet current and future design needs.

REFERENCES

- ABAQUS user's manual 6.3, 2002.
- Agarwal H, Gokhale AM, Graham S, Horstemeyer MF. Material Science and Engineering 2003; A341: 35-42.
- Bammann DJ, Aifantis EC. Nuclear Engineering and Design 1989;116: 355-362.
- Bammann DJ, Chiesa ML, Horstemeyer MF, Weingarten LI. eds. N. Jones and T. Weirzbicki, Structural Crashworthiness and Failure, Elsevier Applied Science, 1993.
- Cocks ACF, Ashby MF. Structural Crashworthiness and Failure 1980; 395-402
- Fang H, Horstemeyer MF. Engineering Optimization 2006; 38: 407-424.
- Fang H, Horstemeyer MF. Advances in Engineering Software 2006; 37: 360-369.
- Fang H, Horstemeyer MF. Multidisciplinary Analysis and Optimization Conference 2004; AIAA 2004-4499.
- Fang H, Rais-Rohani M, Liu Z, Horstemeyer MF. Computers and Structures 2005.
- Fang H, Rais-Rohani M, Horstemeyer MF. AIAA/ISSMO Multidisciplinary Analysis And Optimization Conference 2004; AIAA 2004-4487.
- Fang H, Solanki K, Horstemeyer MF. ASME International mechanical Engineering Congress and Exposition 2004; IMECE2004-59123.
- Fang H, Solanki K, Horstemeyer MF. International Journal of Crash 2005; 10: 161-171.
- Gu L, Li G, Yang RJ. SAE World Congress 2004; 2004-01-1124.

Hammi Y, Horstemeyer MF, Bammann DJ. International Journal of Damage Mechanics 2003; 12: 245-261.

Horstemeyer MF. J Comp Aid Matl Des 2003 ; 36 :13-34.

Horstemeyer MF From Atoms to Autos: Part I: Monotonic Loading Conditions, Sandia National Lab 2001: 6.6-11.

Horstemeyer MF, Gohkale AM. Int. J. Solids and Struct 1999; 36: 6-11.

Horstemeyer MF, Wang P. J Comp Aid. Mat Des 2003;36:13-34.

Horstemeyer MF, Lathrop J, Gohkale AM, Dighe M. Theoretical and Applied Fracture Mechanics 2000; 33: 31-47

Jin R, Chen W, Simpson TW. Struct Multidisp Optim 2001; 23: 1-13.

McClintock FA. ASME J. Appl. Mech. 1968; 35: 363-371.

MathWorks, MATLAB R2007a 2007.

National Highway Traffic Safety Administration Report 2006.

Saitou K, Izui K, Nishiwaki S, Papalambros P. Journal of Computing and information Science in Engineering 2005; 5: 214-226.

Solanki K, Acar E, Rasi-Rohani W, Eamon C, Horstemeyer MF. AIAA 2007; 2007-2340.

Taguchi G, Taguchi Methods,1993.

United States Automotive Materials Partnership (USAMP). Structural Cast Magnesium Development Project, 2006.

APPENDIX A

FORMULA SAE UPRIGHT LOAD CALCULATIONS

Vehicle Parameters:

$W := 550\text{bf} + 175\text{bf}$	$W = 3224.96\text{N}$	Weight of car with driver
$d_f := 50\%$		front weight distribution %
$d_r := 50\%$		rear weight distribution %
$z_f := 31.37\text{in}$		Distance from CG to center of Front Wheel
$z_r := 31.5\text{in}$		Distance from CG to center of Rear Wheel
$w_{\text{track}_f} := 52\text{in}$		Vehicle Front Track Width
$w_{\text{track}_r} := 50\text{in}$		Vehicle Rear Track Width
$y_{\text{cg}} := 12\text{in}$		Height of Center of Gravity
ratio := 50%		Front to Rear Weight Distribution

The vehicle parameters are shown in Fig A.1.

Braking Loads: 1.25G Fwd braking acceleration

Calculate reaction forces and friction forces on wheels:

$g_{\text{brake}} := 1.25$ Acceleration under braking in g's

Sum the moment about the front wheel:

$$R_R := \frac{W \cdot (z_f) - g_{\text{brake}} \cdot W \cdot y_{\text{cg}}}{z_f + z_r} \quad R_R = 839.577\text{N} \quad \text{Normal Force on Rear Wheels}$$

$$R_{RS} := R_R \cdot \frac{1}{2} \quad R_{RS} = 419.789\text{N} \quad \text{Normal Force on a Single Rear Wheel}$$

Sum the forces in the y direction:

$$R_F := (W - R_R) \quad R_F = 2385.38\text{N} \quad \text{Normal Force on Rear Wheels}$$

$$R_{FS} := R_F \cdot \frac{1}{2} \quad R_{FS} = 1192.692\text{N} \quad \text{Normal Force on a Single Rear Wheel}$$

$$\mu_{\text{brake}} := 1.25 \quad \text{The friction coefficient between the tires and the road under braking conditions. This will be equal to the acceleration under braking.}$$

$$F_F := R_{FS} \cdot \mu_{\text{brake}} \quad F_F = 1490.86\text{N} \quad \text{Friction Force on Front Tire While Braking}$$

Resolve forces on wheel to center line of the wheel spindle/upright:

$$D_{\text{wheel}} := 20\text{in} \quad \text{Tire Diameter}$$

$$D_{\text{rotor}} := 9.25\text{in} \quad \text{Brake Rotor Diameter}$$

Calculate torque about the wheel spindle:

$$T_{\text{braking}} := F_F \cdot \frac{1}{2} \cdot D_{\text{wheel}} \quad T_{\text{braking}} = 378679.65\text{N}\cdot\text{mm}$$

This torque is transmitted through the brake rotor and caliper. The caliper is mounted to upright.

$$F_{\text{caliper}} := \frac{T_{\text{braking}}}{\frac{1}{2} \cdot D_{\text{rotor}}} \quad F_{\text{caliper}} = 3223.49\text{N} \quad \text{Force on Caliper}$$

The Caliper is secured to the upright by two mounting holes.

$$F_{\text{cal}} := \frac{1}{2} \cdot F_{\text{caliper}} \quad F_{\text{cal}} = 1611.75\text{N} \quad \text{Force on each Caliper Mounting Hole}$$

Free body diagrams of the 1.25G braking load case is shown in Fig A.2.

Corner Loads: 1.5G Left Hand Turn

Calculate reaction forces and friction forces on wheels:

$$g_{\text{corner}} := 1.5 \quad \text{Acceleration while cornering in g's}$$

Sum the moment about the front right wheel:

$$R_{\text{FL}} := \frac{W \cdot \frac{w_{\text{track}_f}}{2} + W \cdot g_{\text{corner}} \cdot y_{\text{cg}}}{w_{\text{track}_f}} \cdot \text{ratio}$$

$$R_{\text{FL}} = 1364.41\text{N} \quad \text{Normal Force on Front Left}$$

Sum the forces in the y direction:

$$R_{\text{FR}} := d_f W - R_{\text{FL}} \quad R_{\text{FR}} = 248.074\text{N} \quad \text{Normal Force on Front Right}$$

Sum the moment about the rear right wheel:

$$R_{\text{RL}} := \frac{W \cdot \frac{w_{\text{track}_r}}{2} + W \cdot g_{\text{corner}} \cdot y_{\text{cg}}}{w_{\text{track}_r}} \cdot \text{ratio}$$

$$R_{\text{RL}} = 1386.73\text{N} \quad \text{Normal Force on Rear Left}$$

Sum the forces in the y direction:

$$R_{\text{RR}} := d_f W - R_{\text{RL}} \quad R_{\text{RR}} = 225.747\text{N} \quad \text{Normal Force on Front Right}$$

$$\mu_{\text{corner}} := 1.5$$

The friction coefficient between the tires and the road under cornering conditions. This will be equal to the acceleration during turning.

$$F_{\text{FL}} := R_{\text{FL}} \mu_{\text{corner}} \quad F_{\text{FL}} = 2046.61\text{N} \quad \text{Friction Force on Front Left Tire}$$

Resolve forces on wheel to center line of the wheel spindle/upright:

$$M_{\text{corner}} := F_{\text{FL}} \cdot \frac{1}{2} \cdot D_{\text{wheel}} \quad M_{\text{corner}} = 5.198 \times 10^5 \text{ N}\cdot\text{mm}$$

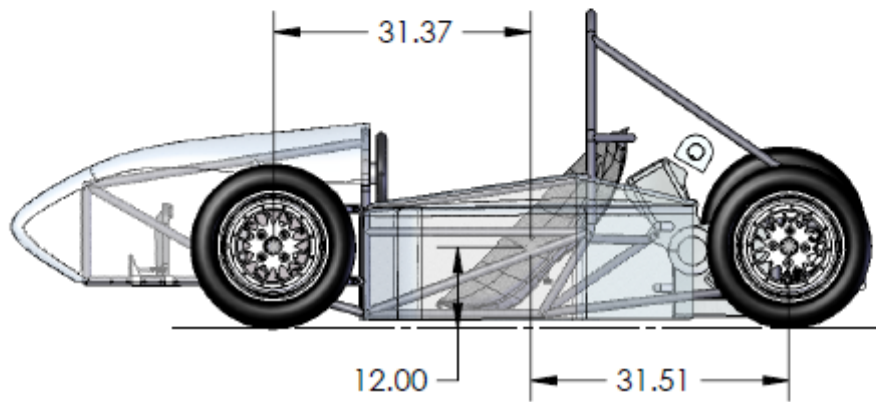
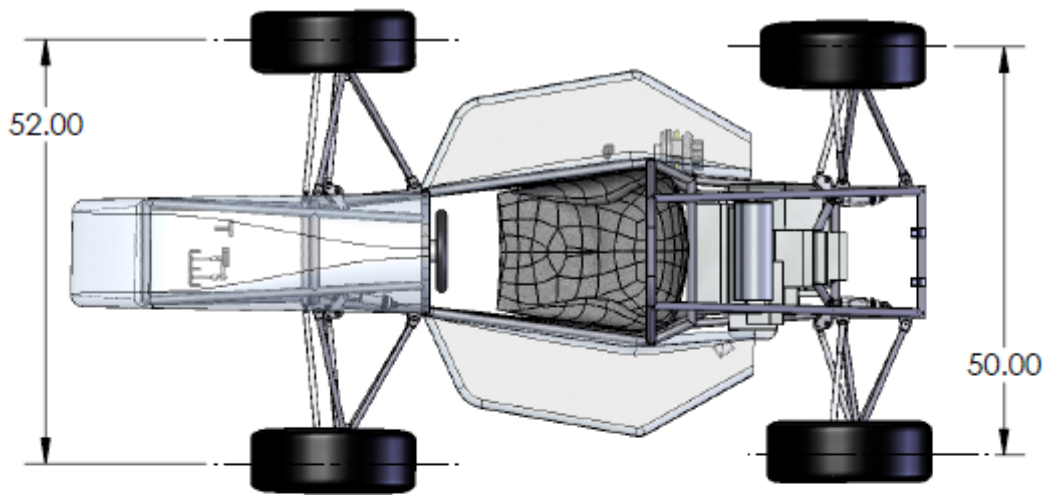


Figure A.1. Vehicle center of gravity location and critical dimensions.

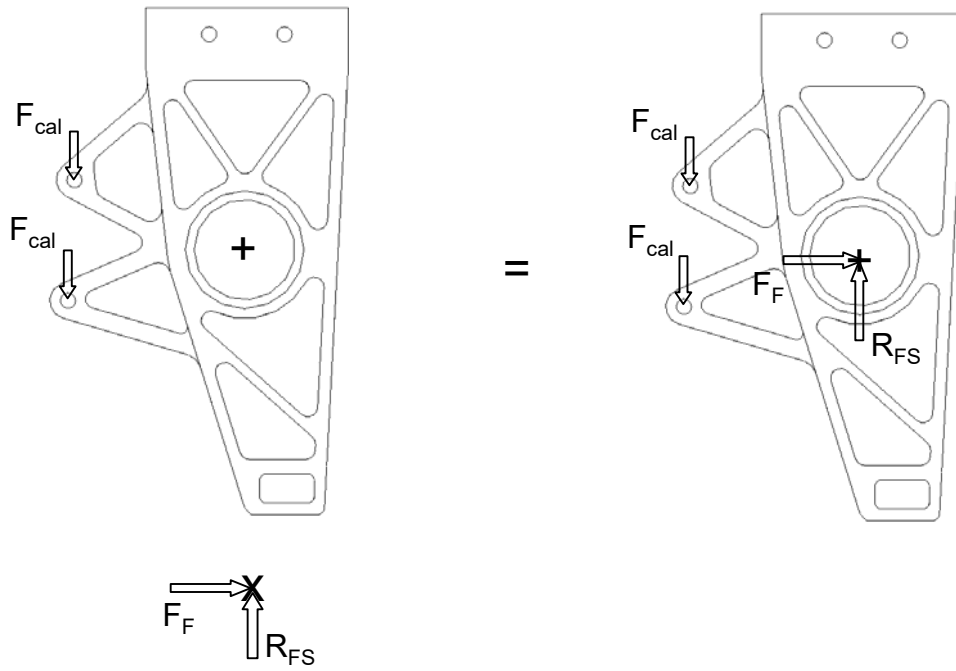


Figure A.2. Freebody diagram of Upright 1.25g Braking Loads.

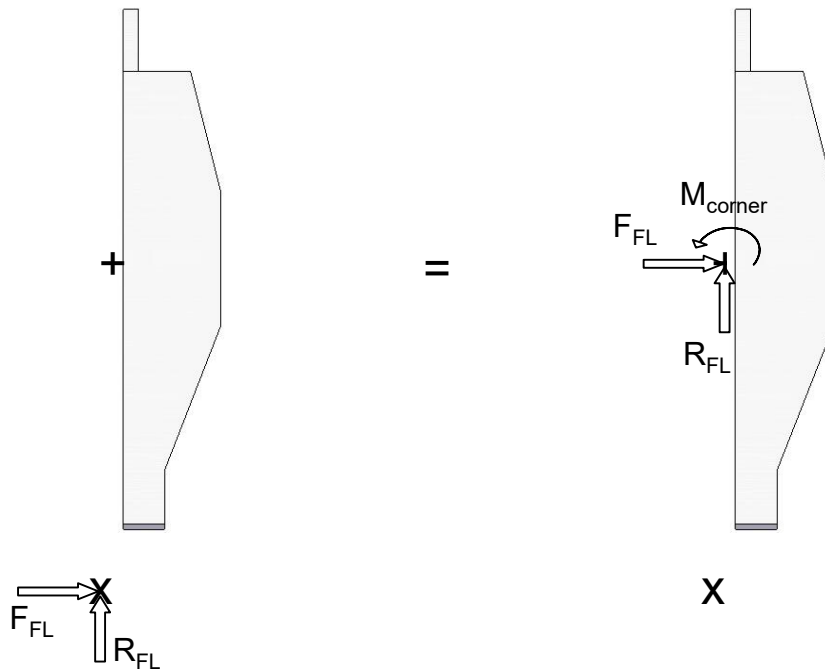


Figure A.3. Freebody diagram of Upright 1.5g Cornering Loads.